High-temperature dust formation in carbon-rich astrophysical environments

Guy Libourel, Marwane Mokhtari, Vandad-Julien Rohani, Bernard Bourdon, Clément Ganino, Eric Lagadec, Philippe Vennéguès, Vincent Guigoz, François Cauneau, Laurent Fulcheri

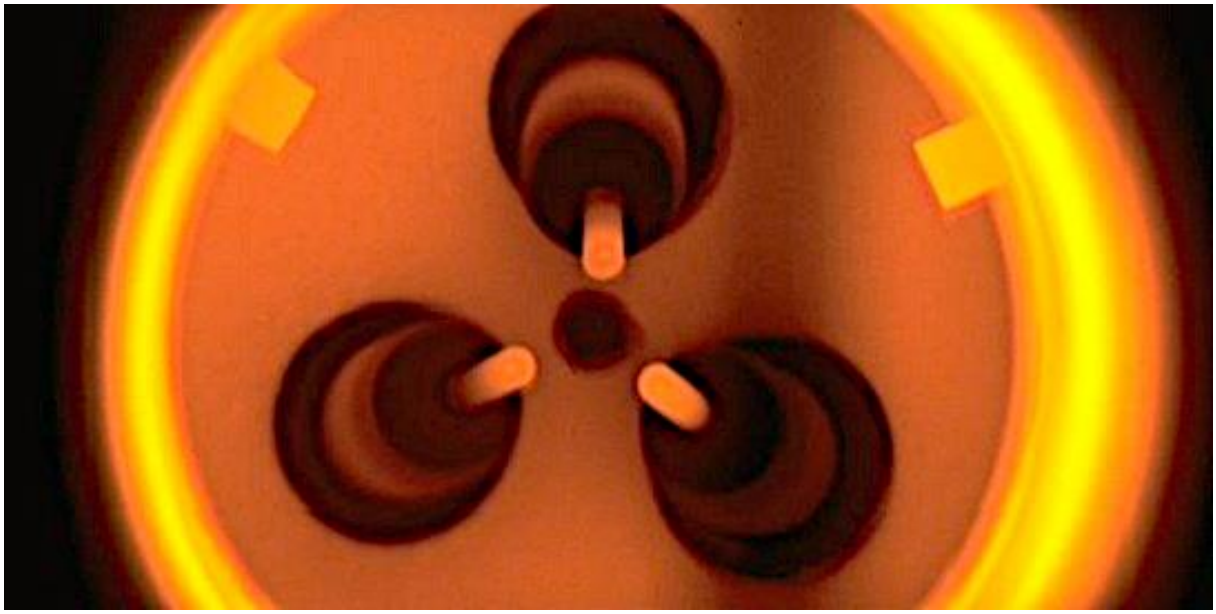

High-temperature dust formation in carbon-rich astrophysical environments

Guy Libourel[1], Marwane Mokhtari[2], Vandad-Julien Rohani[3], Bernard Bourdon[2], Clément Ganino[4], Eric Lagadec[1], Philippe Vennéguès[5], Vincent Guigoz[5], François Cauneau[3], Laurent Fulcheri[3]

[1]Université Côte d'Azur, Observatoire de la Côte d'Azur, CNRS, Laboratoire Lagrange, Boulevard de l'Observatoire, CS 34229, 06304 Nice Cedex 4, France.

[2]Laboratoire de Géologie de Lyon Terre Planètes Environnement, Ecole Normale Supérieure de Lyon, CNRS, Université Lyon I, 46, Allée d'Italie, 69364 Lyon Cedex 07

[3]PSL Research University, MINES ParisTech, PERSEE - Centre Procédés, Énergies renouvelables et Systèmes énergétiques, 1 Rue Claude Daunesse, 06904 Sophia Antipolis, France

[4]Université Côte d'Azur, Observatoire de la Côte d'Azur, CNRS, Laboratoire Géoazur, Sophia-Antipolis, 06560 Valbonne, France

[5]Université Côte d'Azur, CNRS, CRHEA-Centre de Recherche sur l'Hétéro-Epitaxie et ses Applications, Rue Bernard Grégory, 06560 Valbonne, France,

To be submitted to: *Nature Astronomy*

Corresponding author: libou@oca.eu

Abstract:	177	words
Text:	3934	words
Figure:	6	items

+ Extended Data

Abstract

Condensation processes, responsible for the main chemical differences between gas and solids in the galaxy, are the major mechanisms that control the cycle of dust from evolved stars to planetary systems. However, they are still poorly understood, mainly because thermodynamics and kinetic models of nucleation or grain growth are lacking experimental data. To bridge this gap, we used a large volume three-phase AC plasma torch to obtain a full high temperature condensation sequence at elevated C/O ratio from a fluxed chondritic gas composition. We show that the crystallized suites of carbides, silicides, nitrides, sulfides, oxides and silicates and the bulk composition of the condensates are properly modelled by a kinetically inhibited condensation scenario controlled by the gas flow. This validates for the first-time thermodynamic predictions of condensation sequence at high C/O ratio. On this basis and using appropriate optical properties, we also demonstrate the influence of pressure on the dust chemistry as well as the low probability of forming and detecting iron silicides in asymptotic giant branch (AGB) circumstellar environments as well as in our chondritic meteorites.

Introduction

Cosmic dust is of crucial importance for the evolution of our galaxy since it actively participates in the cycle of matter (gas and dust) from the interstellar medium (ISM) to stars and back from stars to the ISM[1]. Dust grains form principally in the gas outflowing from evolved stars and in the ejecta resulting from supernova (SN) explosions. Amongst progenitors, AGB stars are assumed to be the major contributor to the global cosmic dust budget[2]. During their late evolutionary stages, low- and intermediate-mass stars (< 8 $M_{\odot}$) become red giants, increasing their radius by 2-3 orders of magnitude, and decreasing their surface temperature to 2000-3000 K. Further evolution of these stars (AGB phase) lead to significant mass loss of gaseous molecules and dust grains giving rise to circumstellar envelopes (CSE). Mass-loss rates of AGB stars, determined with various observational methods, are typically in the range of 10^{-8}–10^{-5} $M_{\odot}$. $year^{-1}$ but values as high as 10^{-4} $M_{\odot}$. $year^{-1}$ have been found for more extreme objects[3]. Around cool stars, dust is formed in dense shells created by stellar pulsations or large-scale convective motions which propagate gas beyond the stellar surface[4] where gas cooling yields dust condensation. These dust grains are then accelerated away from the star by radiation pressure, dragging the gas away through friction, creating outflows with typical velocities of 5–30 km/s and eventually feeding the ISM[5] contributing thus to the material out of which our solar system formed.

Dust forms from the matter already present when the stars formed and from the elements produced by the stars themselves. The dust composition changes as the star evolves and notably when the carbon to oxygen ratio changes during the episodic third dredge-up process[6]. Thermodynamic equilibrium calculations have provided convincing explanations of the marked chemical differentiation between oxygen-rich and carbon-rich AGB stars based on the high bond energy of carbon (i.e., 1077 $kJ.mol^{-1}$ ≈ 11.1eV[7]) and that CO is a very stable gaseous molecule at relatively high temperatures. Consequently, the dust chemistry in the inner CSE of AGB stars, $R = 1-10R_{*}$ where R_{*} is the stellar radius, is primarily controlled by the carbon-to-oxygen ratio. When C/O ≤1 (O-rich stars), all carbon is bound in the CO molecule and the oxygen in excess participates to oxygen-rich dust formation[8]. In contrast, when C/O ≥1 (C-rich stars) carbon is in excess while all the oxygen is bound in CO and hydrocarbons molecules and carbon-rich grains are formed[9,10]. While the C/O ratio likely explains the fundamental

difference between C-rich and O-rich stars, temperature and pressure within their inner circumstellar envelopes (CSEs) play obviously a significant role (see below).

Complex dynamical effect in stellar outflows[3] and highly diverse circumstellar O-rich and C-rich grains inventory in chondrite meteorites[11,12] highlight, however, the need to consider beyond simple thermodynamic equilibrium in order to understand dust formation around AGB stars, including kinetics, nucleation/seeding processes and models like chaotic solid formation[8,13, 14,15]. This issue has been already the subject of extensive theoretical works[13]. Ref[16] recently re-emphasized the importance of kinetics for dust formation in astrophysical environments, and the need for laboratory condensation experiments to provide insights into the formation of dust and the reactions that allow their growth. While nucleation and growth of simple metal or H_2O grains from a gas have been extensively studied for applications in atmospheric or material science[17,18,19,20,21], condensation of more complex gas, such as those of stellar outflows, is less well studied. The difficulty resides in simulating astrophysical conditions in the lab: (1) producing a multi-elemental refractory gas of controlled composition and (2) condensing it in equilibrium/disequilibrium conditions at very high temperature[22,23,24,25]. Several conditions need indeed to be met for dust/condensed matter formation, such as densities above a certain threshold to ensure sufficient collisions between the constituent particles, moderate temperatures below the stability threshold of the dust component, and sufficient time for the nucleation and growth of molecular clusters into larger grains.

Here 600 g of a 20 µm-sized powder of NWA869 ordinary chondrite have been processed for an hour inside a large volume 250 kW three-phase alternating current (AC) plasma torch with hot graphite electrodes operating at PERSEE, Mines-Paris-Tech, Sophia-Antipolis, France (Fig. 1). Chondritic dust particles were injected using argon gas for propulsion into a 5000 K H_2-Ar admixture gas plasma formed between three graphite electrodes (see Methods). The vapor formed in the plasma flew downwards in a cylindrical meter-sized graphite-coated chamber in which condensation occurred according to the thermal gradient at a pressure $\approx 10^5$ Pa. Nitrogen was injected during the run to avoid hydrogen flammability. The experiment was terminated by shutting down both the electrical power and the powder supply.

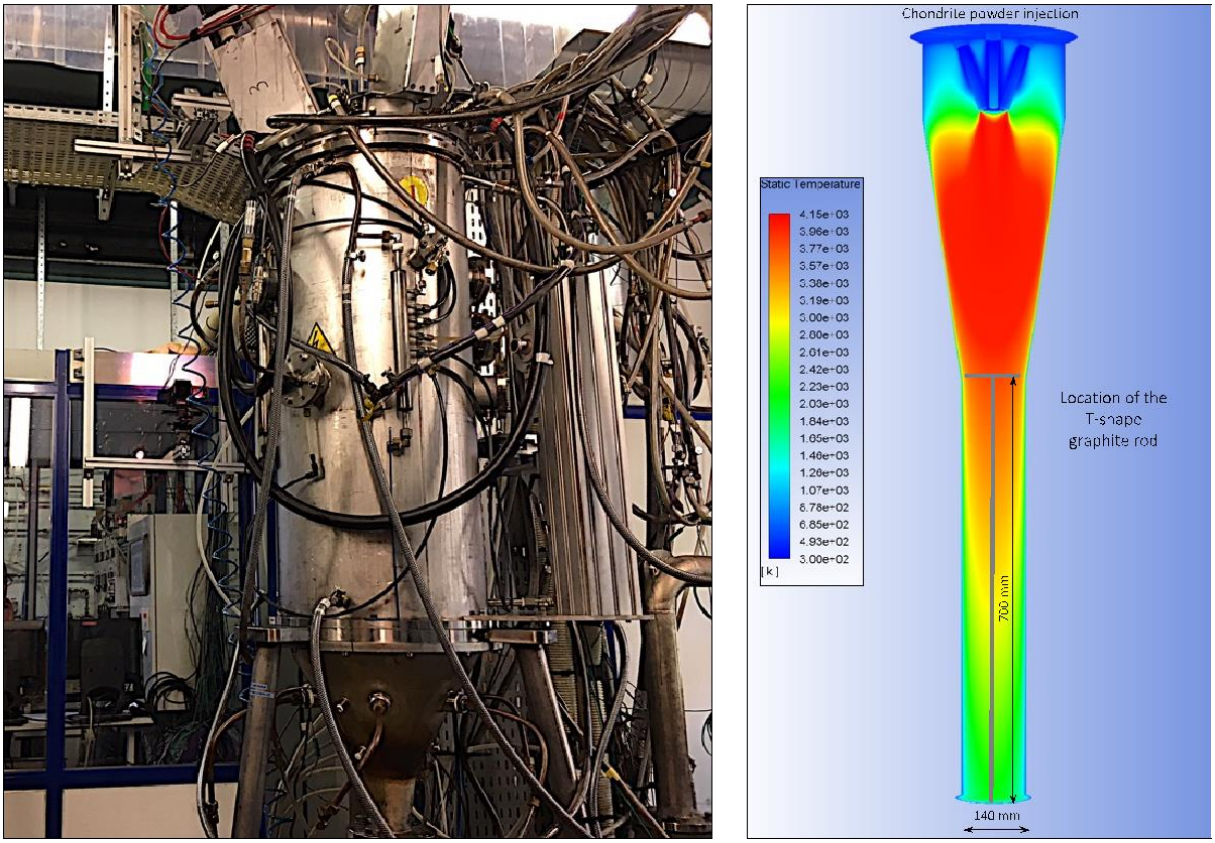

Fig. 1: a) 240kW three electrode arc plasma torch (PERSEE, Mines ParisTech, Sofia-Antipolis, Nice) in which 600 g of a 20 µm-sized powder of NWA869 ordinary chondrite have been processed for an hour. b) Simulated 3D thermal regime inside the condensation chamber using the ANSYS Fluent computational fluid dynamic software. A removable T-shape graphite rod was placed at the center of the chamber and was recovered after the experiment for chemical and mineralogical analyses of the condensates. The 3D simulation was performed in a computational domain that does not explicitly incorporate the T-shape graphite rod. To account for the rod's presence, the torch power was set to the experimentally determined value, maintaining the appropriate source temperature while ensuring overall energy balance. To achieve this, losses induced by the rod were redistributed onto the walls of the chamber, preserving the global thermal behavior of the gas flow. While the thermal distribution may not be locally exact near the rod location, the rod temperature can be considered to lie within the thermal boundary layer that forms near the walls. Equivalence calculations suggest that the rod temperature is approximately between 1/8 and 1/6 of the nozzle diameter away from the walls.

A removable T-shape graphite rod was placed at the center of the chamber and was recovered after the experiment for chemical and mineralogical analyses of the condensates (Fig. 1 and Extended Data Fig. 1). Even if this experiment remains far from CSE conditions, e.g., $P << 10^2$ Pa, which are technically impossible to achieve at present, we show in the following how such high temperature condensates resulting from fluxed chondritic gas at atmospheric pressure in a severe thermal gradient help us to put stringent constraints on dust formation in stellar outflows.

Fig. 2: Photographs of the condensates on T-shape graphite rod after experiment. Notice the change of the structure (e.g., wetting, flaking) and the grain size of the condensates from top (high temperature) to bottom (low temperature). See text.

Results

Owing to this large volume device, the recovery of several hundred grams of high temperature condensates obtained at high C/O ratio is a première. The 3D thermal regime inside the chamber as well as the trajectory and velocity of fictive particles (Fig. 1 and Extended Data Fig. 1) have been obtained using the ANSYS Fluent computational fluid dynamics software (see Methods[26]). While condensation occurred in the whole condensation chamber, the T-shape graphite rod holder offers enough material (Fig. 2) to detail the chemistry (Extended Data Table 2) and the mineralogy (Extended Data Table 1) of the condensates between 2400 K to 1300 K at ambient pressure and C/O ratio ≈ 0.93. The high C/O ratio is due to and regulated by the consumption of graphite from the 3 electrodes during the experiment (see Methods and discussion below).

X-Ray diffraction (XRD) pattern and secondary electron (SE)- and back scattered electron (BSE)-Scanning Electron Microscopy (SEM) characterization reveal that condensates obtained at the highest temperatures, i.e., >2050 K, are dominated by iron silicides (Fe_xSi_y with x/y atomic ratio ≈ 1.2). They formed millimeter-sized droplets wetting the T-shape graphite rod

(Fig. 2). Well crystallized SiC are bathed in the silicides together with rarer and smaller crystals of Al_4SiC_4 and TiC (Fig. 3 and Extended Data Fig. 3).

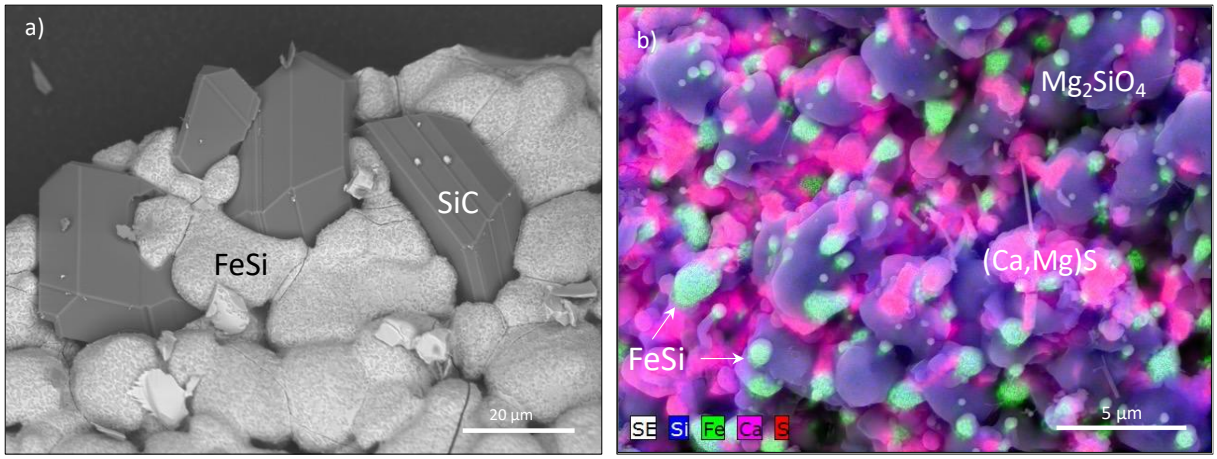

Fig. 3: Representative scanning electron microscope images of high temperature condensates obtained at high C/O ratio. a) Well crystallized SiC bathed in molten FeSi (now solid) from sample #13 condensed at temperature around 2150K. b) Overlapped X-ray elemental map in Ca (pink), Fe (green), Si (blue) and S Kα (red) and SE map of # 8 condensates obtained at temperature 1700K showing an association of oldhamite (CaS-MgS), Mg-rich olivine (Mg_2SiO_4) and molten droplets of iron silicide (FeSi).

A temperature of about 2050 K marks the onset of condensation of oxygen-bearing and sulfur-bearing phases with the occurrence of calcium-aluminate (silica poor) glass and of CaS-MgS oldhamite, respectively. Calcium-aluminates, that are initially molten, wet the immiscible FeSi molten droplets and most of the already condensed crystalline phases, including SiC. Oldhamite condenses first as Ca-rich phase and shifts to an MgS-rich composition as temperature drops. AlN (some of which are whiskers) and TiN nitrides appear below on the T-rod in a narrow interval of temperature between 2000-1900 K. In the same range of temperature, olivine Mg_2SiO_4 starts to crystallize from the melt (now glassy and enriched in MgO and SiO_2) in close association with FeSi and SiC. Below a temperature range of 1850-1800 K, X-ray diffraction analysis reveals a critical shift in the condensate composition. Graphite becomes the dominant phase, while carbides are no longer detectable. Low Ca-pyroxene $MgSiO_3$ starts to condense below 1700 K forming remarkable 1-D whiskers by a FeSi catalyst-assisted VLS (vapor-liquid-solid) growth process as shown in the Extended Data Fig. 3. Iron silicides, Fe_xSi_y have x/y atomic ratio close to 2 in these low temperature condensates. Crystals of periclase MgO have also been found in the lowest temperature part of the condensates. Finally, a clear decrease by one order of magnitude in the average size of condensed phases from tens of microns to tens of nanometers is noticeable as condensation temperature drops from top to bottom of the T-shape graphite rod.

Extended Data Table 1 shows the bulk chemistry (Si, Ti, Al, Ca, Mg, Fe, Mn, Na, K, P, C and S) of both the starting NWA 869 chondrite composition as well as the 14 aliquots of condensates sampled on T-shape graphite rod holder measured by Inductively Coupled Plasma Optical Emission Spectrometry (ICP-OES).

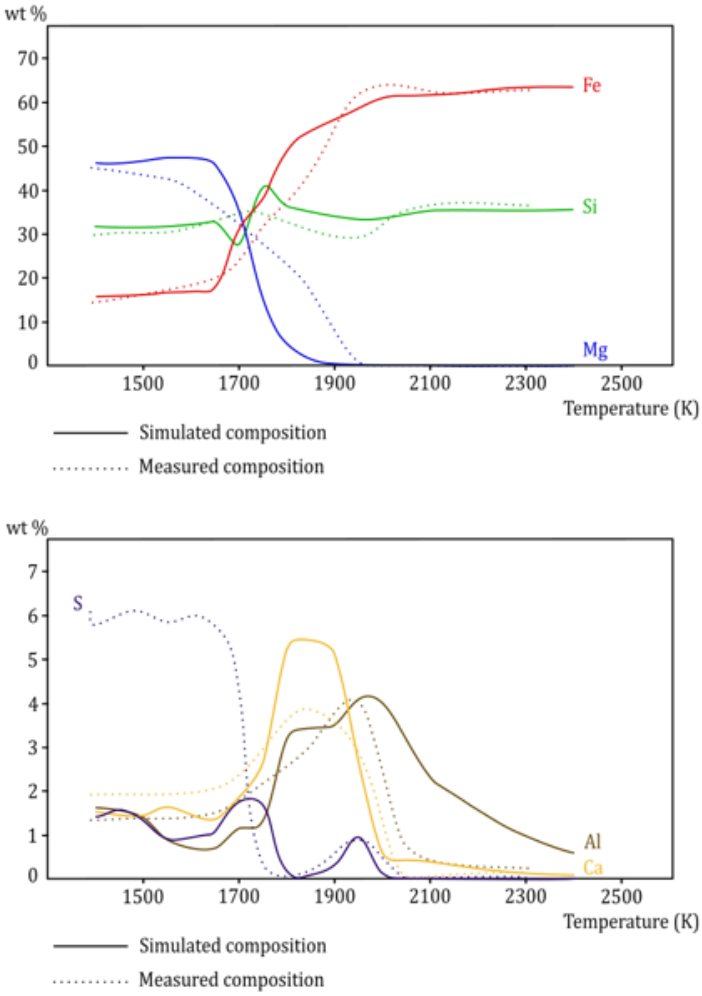

Fig. 4: Composition patterns for the main major and minor elements of the condensates considering a kinetically limited condensation with various *f* values for the phases (see text). The solid lines correspond to the modeled compositions and the dashed lines to the measured ones.

As condensation proceeds downward in the chamber, condensates are first enriched in Fe, Si, Ti and C, then become enriched in Al, Ca, S, and next in Mg, a change in chemistry in good agreement with their mineralogy (Fig. 4). Sulfur is however enriched in the low temperature condensates (< 1600 K). Only trace amounts of Na are found in the lowest temperature condensates while K is totally absent of this high C/O ratio condensation sequence.

Discussion

A. Laboratory condensation of chondritic gas at high C/O ratios

Our results show a sequence of carbides, sulfides, nitrides, and oxides that are generally consistent with calculations made in previous studies that correspond to the low-pressure conditions of protoplanetary disks or stellar atmospheres at high C/O ratios[14,27,28,29,30]. However, there are some differences due to the duration and the high-pressure conditions ($\approx 10^5$ Pa) of the experiment. Carbon in our experimental condensates is mainly in the form of carbides at high temperatures (above 1850 K) and transitions to graphite at lower temperature.

No evidence of amorphous carbon has been found. The most important difference is the stability of liquids in these conditions, namely iron silicide metallic liquid and oxide/silicate liquid, which are immiscible with each other. As is well known in materials science, the liquid acting as a catalyst promotes mass transfer in the VLS system and controls the growth and shape of the crystals. The large SiC crystals that crystallize from FeSi liquid[31] and the various 1D crystals/whiskers of AlN, $MgSiO_3$ catalyzed by liquid FeSi droplets on their tips provide convincing examples of the VLS process and its importance at high-pressure condensation conditions (Fig. 3 and Extended Data Fig. 3).

Regarding the chemistry of condensates (Extended Table 1), the calculated compositions based on thermodynamic equilibrium or fractional condensation do not match the measured compositions, while the calculated mineralogical sequences do (see Methods). In other words, this suggests that an equilibrium condensation sequence, i.e., the order of phase appearance during condensation, is not a good discriminant for identifying the exact process of condensation (see below). We thus explore a partial fractional condensation model (Extended Data Fig. 4) where only a fraction *f* of what was expected to condense in equilibrium could effectively condense due to kinetic limitations (See Methods).

The condensation pattern of Si, Fe, Al and Ca determined with the model fits well with the experiments (Fig. 4). Fe concentrations in the condensates remain high (~ 60 %) until 1950 K, when phases other than FeSi start condensing (SiC, AlN, CaS, oxide melt). The modelled x/y ratio of the Fe_xSi_y molten alloy ranges from 1 to about 2 as the temperature decreases, which is perfectly consistent with the measured compositions. The Si concentration remains almost constant along the rod, showing a roughly constant condensation of this element in various phases: FeSi, SiC, oxide melt, followed by silicates. Ca concentration shows a sharp increase until CaS becomes stable (Fig. 4). Its concentration increases until it reaches a maximum at 1900 K. At this temperature, CaS is no longer stable, and Ca is mainly partitioned in the oxide melt. Al concentrations show a rather similar pattern, with a sharp increase when AlN becomes stable, followed by a short decrease until it reaches a plateau at 1900 K when AlN is no longer stable, and Al condenses in the oxide melt. Both Ca and Al concentrations sharply decrease after 1800 K when Ca-poor and Al-poor phases start condensing (i.e., olivine and periclase).

Despite the overall good agreement, some discrepancies between the model and the experiment can be observed (Fig. 4). The main issue is related to sulfur which has very low predicted concentration in the low-temperature sections compared with the measured concentrations. The main S-bearing phase in the thermodynamic simulations is CaS, while the experimental results are not consistent with the calculated condensation curve for this species: to obtain a CaS phase, the concentration of Ca should have been much higher than what is observed. Furthermore, no new sulfide phase was identified in the low-temperature segments of the rod with XRD. There is thus a clear problem with the sulfur data that could have arisen for several reasons including i) analytical artifact with the measurement, ii) contamination by the condensation chamber, and iii) thermodynamic underestimation of the amount of S that could get dissolved in the FeSi, and/or iv) significant solubility of sulfur in silicate liquids under reducing conditions[32]. Despite this difference in concentrations, the predicted and observed patterns of S concentrations are very similar, with a first peak of concentration at 1950 K corresponding to the initial stability field of CaS and a sharp increase until a plateau around 1750 K corresponding to the second stability field of CaS.

Our model, which incorporates a kinetically limited condensation mechanism, effectively reproduces the experimental results for most major elements at high C/O ratios. This provides

the first experimental validation of thermodynamic calculations employed to predict condensation sequences under such conditions. Notably, it is also established that the kinetically inhibited condensation sequence does not differ from the equilibrium sequence, whereas the relative abundances of the condensed phases and the resulting bulk composition do. Consequently, the bulk composition, rather than the mineralogical sequence of condensation, serves as a more reliable indicator of the extent of kinetic limitations during the condensation process.

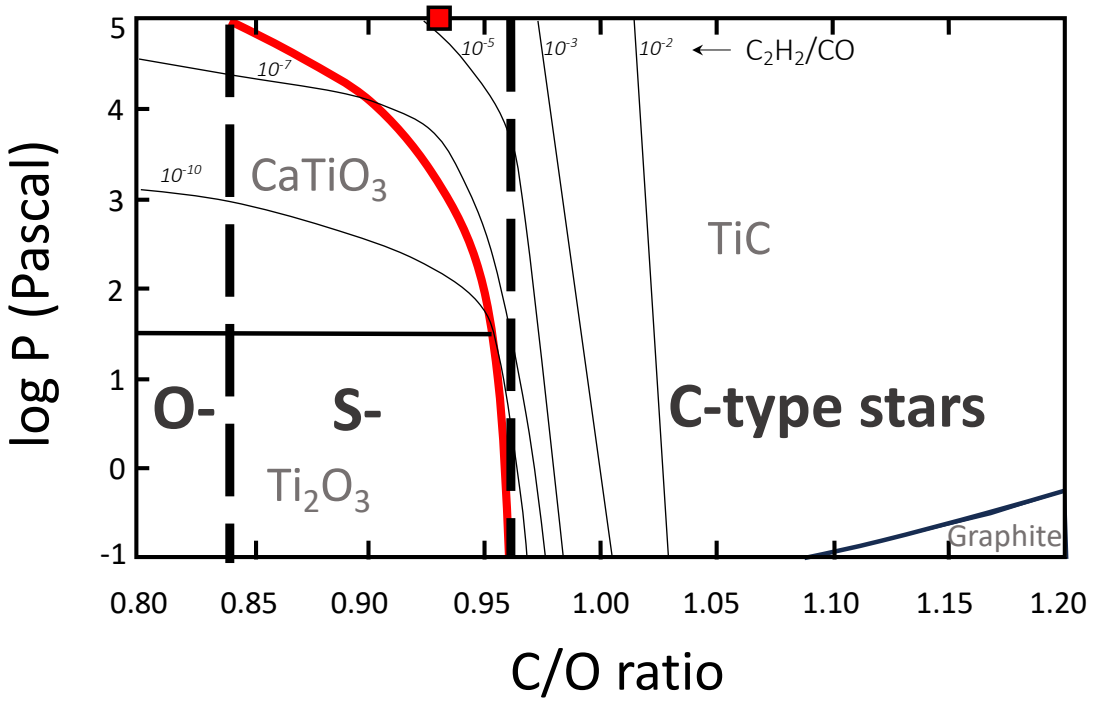

Fig. 5: Pressure versus C/O ratio diagram showing the stability field of first condensates using the starting bulk composition of the solar composition from ref[33], except for the C abundance. In this range of P and C/O ratio, Ti_2O_3 and $CaTiO_3$ are stable at low C/O ratio; note that Al_2O_3 (not shown) is stable at lower C/O ratios[28]. At higher C/O ratio, oxides are no longer stable, and TiC and graphite are becoming predominant. Red square corresponds to our experimental conditions. Thin lines stand for the C_2H_2/CO ratio in the gas phase at the saturation of the first condensates, i.e., Ti_2O_3, $CaTiO_3$, TiC or graphite - depending on the C/O ratio and the pressure. Notice the significant pressure influence of the transition between carbon- and oxygen-bearing phases (red curve). As pressure approaches 10^5 Pa, the C/O threshold drops well below ≈ 1, indicating a strong destabilization of oxide phases in favor of carbides (See text).

It is crucial to highlight that while the traditional distinction between O-rich and C-rich dust chemistry commonly aligns with a C/O value of unity, the C/O ratio derived from our C-rich dust-generating experiment dips below this threshold, settling at C/O = 0.93. This reported ratio is thus typical of a S-type star rather than that of a C-type star. According to previous thermodynamic calculations[28], the transition between reduced phases (e.g., carbides, nitrides) and oxygen-bearing phases (e.g., oxides, silicates) is also observed at a C/O ratio of approximately 0.96 at a total pressure of 10^2 Pa, indicating a significant pressure influence on this transition. This is corroborated by our thermodynamic calculations, as shown in Figure 5. Our results confirm a significant pressure-dependent shift in the C/O value required for oxide formation. As pressure approaches 10^5 Pa, C/O threshold drops well below ≈ 1, indicating a strong destabilization of oxide phases in favor of the carbides. This is concomitant to the

dramatic increase in the proportion of carbon-hydrogen bond as pressure rises, as indicated by the increase of C_2H_2/CO ratio of the vapor phase (Fig. 5). The observed preference for C-H bond formation can be attributed to the inherent weakness of this bond compared to the C-O bond in carbon monoxide. The C-H bond energy is several hundreds of kJ/mol lower, making it significantly easier to break and participate in the formation of new reactive carbon species in the vapor phase under pressure. Such pressure effect can be rationalized by a reaction involving the main gas species of the type:

$$2\ CO_{(g)} + 3\ H_{2(g)} = C_2H_{2(g)} + 2\ H_2O_{(g)}$$

which, according to Le Chatelier's principle, will be shifted towards the product side (C_2H_2 formation) as pressure increases ($P\Delta V$ negative). This aligns perfectly with the observed increasing stability of C-bearing condensed phases at higher pressures and with the presented experimental data (Fig. 5). In light of this, our condensation sequence at 10^5 Pa with C/O = 0.93 replicates the sequence observed in CSE with higher C/O ratios. In what follows, we explore the consequence of our thermodynamic calculations extended to low-pressure conditions that are representative of stellar atmospheres with high C/O ratio such as AGB S- and C-stars.

B. Condensation in C-rich stellar atmospheres

Evolution of AGB stars is controlled by two main processes: dredge-ups that bring material from the inner shell to the most outer layers, thus increasing the C/O ratio of the stellar atmosphere[34,35], and mass loss including C through stellar winds[36]. Dust formation by condensation is crucial since stellar winds are driven by momentum transfer from the photons emitted by the star to the surrounding dust[3,37]. The accelerated dust then drags the surrounding gas and stellar winds are formed. The acceleration of dust by radiative pressure depends on the efficiency of the momentum transfer from the photons to the grains, namely the mean opacity of the dust. Stellar winds can only form if the radiative pressure force exceeds the local gravity force of the star, which is when the mean opacity of the dust exceeds a critical value that depends on the star mass and luminosity. However, momentum transfer is not the only light-matter interaction that plays an essential role. In particular, the light absorption properties of some minerals can heat up the grains such that the actual temperature of the dust grains can be different from the local gas temperature. Thus, these grains can be heavily heated up and their temperature can then exceed their condensation temperature. Consequently, their condensation can be inhibited, destabilizing these minerals even though the gas temperature should allow condensation. This phenomenon has already been described for Fe-bearing olivines around AGB M-stars[38]. This effect will contribute to increasing the effective oversaturation of this phase. As the gas and dust flow away from the star, the temperature and pressure decrease such that at some point the predicted dust temperature shall correspond to its condensation temperature[39,40]. The evolution of the AGB stars critically depends on the properties of the condensing grains with respect to light-matter interactions. According to ref[39], the degree of heating of a mineral phase will depend on a parameter p whose value can be calculated if the dependence of the coefficient of absorption Q_{abs} as a function of wavelength is known. The values of p for mineral phases predicted in our condensation sequence were calculated based on their optical properties (whenever they were not directly available from the literature) and are reported in Extended Data Table 4. The p values were used to compute the actual temperature of the dust as a function of the distance from the star[40] (See Methods).

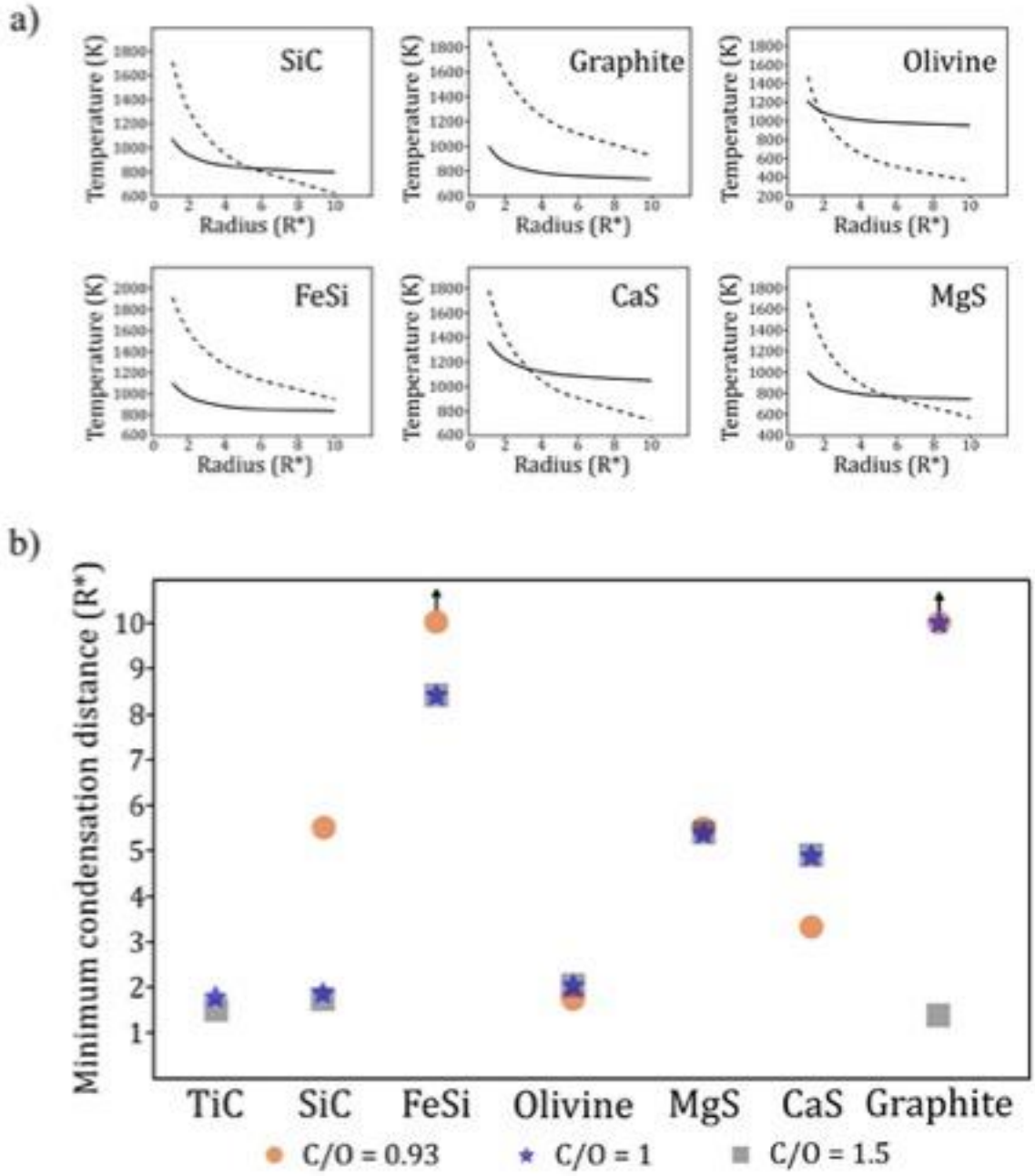

Fig. 6: a) Comparison of the thermodynamic condensation temperature (solid line) and the dust temperature (dashed line) as function of the distance from an AGB star with a C/O ratio of 0.93 for six different minerals. The composition of the gas and the pressure profile are from ref[14]. The surface temperature of the star is considered to be 2500 K. Condensation of minerals can only occur when the actual dust temperature is lower than the condensation temperature, i.e the minimum condensation distance is the intersection of the dashed line and the solid line. b) Condensation distances for various mineral phases calculated for C/O of 0.93, 1 and 1.5. The distances are expressed as multiples of the star radius and were obtained using the same approach as in a).

The condensation temperatures of dust with a C-star composition were then calculated using the same thermodynamic database as that used for modeling our experimental condensation sequence. The starting bulk composition was the solar abundance from ref[33] with an increased C abundance. The distance where a mineral first condenses was calculated for a temperature

and pressure profile in the extended atmosphere of a representative AGB star[14]. In this calculation, the abundance of C was increased over the solar value starting from a value of 0.93 (corresponding to our experiment) up to 1.5, since most C-rich AGB stars have 1< C/O < 1.5. The results of these calculations were then plotted in Figure 6 where dust temperatures are also reported. In principle, the minimum distance where dust can condensate is located at the intersection of the condensation temperature and dust temperature curves. For TiC, SiC and olivine, the distance is close to the star (<2R$_*$). In these conditions, the pressure is high enough (>10^{-2} Pa) for condensation to occur. However, for CaS, FeSi and C, the condensation can only take place at distances greater than 5R$_*$. At this distance, the pressure is lower than 10^{-5} Pa and the condensation must take place at a much lower rate owing to a lower local density. In order to further determine whether the formation of FeSi dust could take place despite the low density at such a large distance from the star, we evaluated the timescale necessary for FeSi dust growth compared with the timescale of the outflow itself using the approach described in ref[41] using an appropriate set of parameters (See Methods). The results are shown in Extended Data Fig. 5. The growth timescale for dust particles between 10^{-1} and 10^{-3} µm is always an order of magnitude longer than the outflow timescale. This shows that provided the dust temperatures prevent condensation at a close distance from the star (here >5R$_*$), the low density in this environment then becomes prohibitive for allowing a rapid enough grain growth. Consequently, our kinetic models predict that FeSi is unlikely to form in the outflows of C-rich AGB stars, despite thermodynamic predictions favoring its condensation under these conditions. In addition, one could note that the detection of IR signature for FeSi in stellar outflows is itself difficult[42] due to the lack of distinct spectral features.

Assuming that our calculations capture the essence of processing affecting dust generated in C-rich AGB stars, these results can be compared with direct observations of AGB stellar outflows and presolar grains preserved in primitive chondrites. Mid-infrared (MIR) survey of evolved stars has revealed a clear dichotomy in the chemical properties of dusty outflows. Carbon dust, be it amorphous carbon or crystallized graphite[43], and silicon carbide appear together in the outflows of C-enriched stars, whereas silicates, alumina and water ice dominate the dust emission of stars with C/O<<1[44]. C-rich dust, such as graphite, SiC and polycyclic aromatic hydrocarbons (PAHs) do show emission features at 3-30 µm. The carriers of the 21 µm and 30 µm features in the outflows of C-rich stars are currently still debated[45]. For instance, the feature observed around 30 µm in the outflows of C-stars is often attributed to MgS but its formation is unclear[45,46,47]. An important feature is that AGB dust has an extremely low Fe content, although iron is significantly depleted from the gas phase in both circumstellar and interstellar environments and ~90% of iron produced by stars should be in dust grains. These features seem consistent with our modeling, suggesting the absence of FeSi condensation due to kinetic constraints.

Similarly, the mineralogy and composition of presolar grains provide some strong hints about their birth environment. It is commonly considered that the majority of these grains come from C-rich AGB with abundant SiC[48] and rare C[49], CaS and MgS and TiC (but also (Zr,Mo)C has also been documented as tiny grains[50,51,52,53]). In contrast, the presence of FeSi is very rare and only mentioned as a small inclusion by ref[53]. Thus, to a first order, our modeling is consistent with observations in presolar grains. In some cases, TiC has been described as occurring as inclusions inside SiC or graphite dust grains and it has been suggested in previous studies that TiC (or ZrC) could have acted as a seed for heterogeneous nucleation [51,54,55,56,57,58]. This could indeed have been the case when they occur in a central position. However, according to the observations of ref[53], their elongated shape seems to preclude a condensation origin for the TiC inclusions and would suggest also a secondary exsolution.

Conclusion

Overall, our experiment validates the mineralogical sequence that had been predicted by equilibrium thermodynamic calculations and shows that under kinetic conditions where condensation is limited by flow rate, the equilibrium sequence of minerals is preserved, while the phase abundance is under kinetic control. By including the effect of light interaction with minerals that have strong IR absorption, our results also show that one can effectively predict the observed minerals found in C-rich stars, but also in presolar grains. It should be mentioned, however, that wind characteristics of AGB stars could be significantly affected in the case of binary systems with closed-by companions which often have an equatorial density enhancement, accretion disk and complex inner wind dynamics[59]. Nevertheless, this study suggests that more extensive condensation experiments such as that presented here could provide novel insights into dust formation in astrophysical environments.

Methods

A. Experimental approach

The experimental work was performed at Mines ParisTech-PERSEE, Sophia-Antipolis, Nice (Fig. 1). The experimental setup was made of a large volume plasma torch at atmospheric pressure. A finely ground powder (~ 20 µm) of the NWA 869 ordinary chondrite (bulk composition given Extended Data Table 1) was injected in a 5000 K Ar-H_2 plasma formed between 3 graphite electrodes. The total volume of plasma thus formed was about 1 L. Electrode erosion enriched the vapor with carbon, driving a constant C/O ratio near unity. This ratio is significantly higher than the initial C/O ratio of the starting chondritic material. The vapor formed in the plasma flew downwards in a graphite-coated chamber along which condensation occurred in a temperature gradient. A removable T-shaped graphite rod positioned at the chamber's center facilitated the retrieval of condensates formed due to the chamber's thermal gradient. The temperature and flow velocity were determined numerically. The magneto-hydrodynamic equations of the gas as well as the thermo-mechanical evolution of 2000 virtual particles were solved using ANSYS Fluent software[26]. From this, we were able to compute the temperature field inside the condensation chamber (Fig 1.b.) and the gas flow streamlines. The flow velocity ranged between 1 m/s and 0.6 m/s at the top and end of the chamber respectively, while the temperature ranged from 2400 K to 1300 K at the top and end of the graphite rod, respectively. The rod was recovered after the experiment and underwent chemical and mineralogical analyses. Condensates on the T-shaped graphite rod were collected using a scraping technique from fourteen, 5 cm long segments along its length (Extended Data Fig. 2 and Extended Data Fig. 3). The chemical and mineralogical compositions of each segment were then analyzed and are summarized in Extended Data Table 1 and Extended Data Table 2, respectively.

B. Thermodynamic simulations

The thermodynamic simulations of the system were done with the FactSage software. This software computes the equilibrium composition of a system based on Gibbs energy minimization method, given a composition and the P-T conditions of the system. We used the FactPS, FTStel and FToxid databases[60]. By calculating equilibrium phase composition as a function of decreasing temperature, the software is able to simulate condensation starting from a vapor with a chondritic composition, mixed with Ar, N_2, H_2 and additional C.

The system was composed of 600 g of the NWA 869 composition (Extended Data Table 1) and an amount of Ar, H_2 and N_2 that correspond to the total amount of gas flowing in the plasma torch during the experiment. As the actual C/O ratio of the system could not be easily determined, several simulations were performed with a C/O molar ratio ranging from 0.72 to 1.15. For each simulated composition, the pressure was kept at the constant value of 10^5 Pa whereas the temperature ranged between 2700 and 1300 K with temperature steps of 50 K.

For each temperature step, the software computed the expected phases in equilibrium, including their composition and total masses. We considered three possible condensation behaviors: an equilibrium condensation where the bulk composition of the system remained constant along its path, a fractional condensation where all the condensed material was subtracted from the vapor composition at each temperature step and a partially fractional condensation where only a fraction f of what was supposed to condense at equilibrium could effectively condense due to kinetic effects (see section C. below). For each of these scenarios, we were able to define a condensation sequence and the bulk chemical pattern of the condensates with decreasing temperature. These results were then compared with the actual sequence and the chemical pattern measured on the T-shape rod.

C. Thermo-kinetic model of condensation

Since the data could not be explained by an equilibrium model or a fractional condensation model, we designed a kinetic model that considers the kinetics of condensation as the vapor is flowing through the condensation chamber. The schematic geometry of the experiment is presented in Extended Data Fig. 3. The system is composed of the condensation chamber with a radius r = 7 cm. At the center of the chamber, the rod is assumed to be a cylinder with a radius r' = 1 cm. Only a fraction f of what was expected to condense in equilibrium could effectively condense due to kinetic limitations. To evaluate a value of f that would be consistent with kinetic constraints, we included a model for gas flow through the graphite-coated chamber. We considered that the kinetics of condensation was controlled by gas flow, thus neglecting the kinetics of nucleation. The vapor was assumed to flow downward through a vertical cylinder of diameter r. If one considers a slice of thickness dz through the cylindrical tank located below the plasma, one can write a mass balance equation for the fluxes (Extended Data Fig. 4):

$$F_{in}(z) = F_{out}(z + dz) + F_{cond}(z) \quad (1)$$

where F_{in} is the advective flux of gas entering at position z, F_{out} is the advective flux of gas leaving at position $z+dz$ and F_{cond} is the condensation flux on the chamber's inner surface.

One can then write F_{in} and F_{out} as a function of the molecular densities $\rho(z)$ and $\rho(z+dz)$ respectively:

$$F_{in}(z) = \rho(z)Sv$$

$$F_{out}(z + dz) = \rho(z + dz)Sv$$

S is the surface of an axial section through the system, i.e., $S = 2\pi(r^2 - r'^2)$, v is the mean vertical gas velocity. The condensation of elements follows the Hertz-Knudsen equation:

$$F_{cond}(z) = \frac{S'\alpha(P_i(z) - P_{i,sat}(z))}{\sqrt{2\pi MRT(z)}}$$

S', the total condensation surface, is made of the rod and the chamber sides, *M* is the molar mass of the evaporated species and α is the condensation coefficient (or sticking coefficient). For a small slice of length *dz*, the total condensation surface is S'= 2π(r+r') dz.

Considering the vapor phase as an ideal gas, one can write: $\rho_i(z) = \frac{P_i(z)}{RT(z)}$

The flux conservation equation thus becomes:

$$\rho_i(z)Sv = S' \frac{\alpha\left(P_i(z) - P_{i,sat}(z)\right)}{\sqrt{2\pi MRT(z)}} + \rho_i(z+dz)Sv$$

This equation can be further transformed as follows:

$$\left(\frac{P_i(z)}{RT(z)} - \frac{P_i(z+dz)}{RT(z+dz)}\right)Sv = \frac{S'\alpha\left(P_i(z) - P_{i,sat}(z)\right)}{\sqrt{2\pi RT(z)}}$$

$$\frac{d\left(\frac{P_i}{T}\right)}{dz}dz = \frac{2\pi(r+r')dz\,\alpha\left(P_i(z) - P_{i,sat}(z+dz)\right)}{Sv}\sqrt{\frac{R}{2\pi MT(z)}}$$

$$\frac{T(z)\frac{dP_i}{dz} - P_i\frac{dT}{dz}}{T^2(z)} = \frac{2\pi(r+r')\alpha\left(P_i(z) - P_{i,sat}(z)\right)}{Sv}\sqrt{\frac{R}{2\pi MT(z)}}$$

The final equation is then written and can be integrated numerically:

$$\frac{dP_i}{dz} = \frac{2\pi(r+r')\alpha\left(P_i(z) - P_{i,sat}(z)\right)}{Sv}\sqrt{\frac{RT(z)}{2\pi M}} + \frac{P_i}{T(z)}\frac{dT}{dz} \qquad (2)$$

The first term of the right-hand side of the equation corresponds to the condensation flux and the second term is the pressure variation linked to the temperature gradient *dT/dz*, which was computed with the calculated temperature from the Fluent software. The saturation pressures for the different species in the gas phase were evaluated with the equilibrium values calculated with FactSage.

Equation (2) was integrated numerically to calculate $P_i(z)$ based on the computed thermal gradient and the vapor pressure $P_{i,sat}$ that was calculated in the thermodynamic simulations described above. For the sake of simplicity, we focused on elements with a reduced number of species in the vapor phase and which condense in a reduced number of phases, such as $Fe_{(g)}$ which condenses in the FeSi molten alloy. We also applied this model to $Si_{(g)}$ in the upper part of the rod, as it condenses in the FeSi alloy as well, and $Ca_{(g)}$ which condenses only in the oxide melt and in the oldhamite when T > 1600 K. The fraction of element *i* that effectively condensed relative to the maximum amount that would have condensed, had we reached chemical equilibrium, can be expressed as:

$$f_i = \frac{n_i(T) - n_i(T+\Delta T)}{n_i(T) - \overline{n_{i,sat}}(T)} \qquad (3$$

where $n_i(T)$ is the number of moles of *i* at temperature T and $\overline{n_{i,sat}}(T)$ is the mean number of moles of i in equilibrium over the [T, T+ΔT] interval with ΔT = 50 K. Our thermodynamic calculations show that $\overline{n_{i,sat}}(T) \ll n_i(T)$ at all temperatures in the experiment. Thus, the value of f_i can be approximated with:

$$f_i \approx \frac{n_i(T) - n_i(T+\Delta T)}{n_i(T)} \qquad (4)$$

The f_i value depends implicitly on the oversaturation of a species $P_i/P_{(sat,i)}$ in the vapor and on the condensation coefficient α, which is a critical parameter to compute the value of f_i. The condensation coefficient of iron was determined experimentally[19] at pressures lower than those of our experiment and reported a value of 1 for oversaturation greater than 10. However, it has been shown for other elements that the condensation coefficient decreases with pressure. The measured chemical pattern of Fe (Fig. 4) is best fit by an f value of 6 to 8%, corresponding to an α value of 0.4, which is within the range of condensation coefficients reported in ref.[19]. For calcium, a value of 0.2 for α_{Ca} yielded the best fit, which is consistent with published data for Ca evaporation[61,62] and with the mean value for divalent cation evaporation from silicate melt[63,64], especially in H-rich environment[61]. The α_{Si} is poorly constrained from previous work and its value was adjusted to 0.45. The values of the condensation factors f are reported in Table S3 for the various types of condensates. A best fit was obtained with a constant condensation fraction for all chemical species of a given phase. For all the elements, we found f_i values well below one (see Extended Data Table 3), expressing the kinetic limitation in the condensation rate due to the effect of gas flow and kinetic barrier represented by the condensation coefficient α_i.

As shown in Extended Data Fig. 4, the condensation fraction f of Fe assessed with this model shows a moderate increase from 6% at 2280 K to 8.2% at 1377 K with a mean value of 7%. The computed f_{Si} value shows the same pattern with temperature, with a mean value equal to 8.3% in the region in which Si condenses in the FeSi metal. For Ca, two regime stages of condensation were considered: the first region where Ca only condenses only in the oxide melt (T>1750 K) and second a region where Ca condenses both in the silicate melt and in the sulfide phase (T<1750 K). This leads to a concave curve with an increase of f_{Ca} from 1.5% at 1950 K to 2.6% at 1618 K. Finally, the f factor of the different phases used for the thermodynamic calculations are presented in Extended Data Table 3.

D. Optical properties and condensation distances

The condensation of dust in the outflow of C-rich stars should to some extent be controlled by the thermodynamics of solid phase formation with a vapor composition at a high C/O ratio. However, it has been shown in several studies[65] that the radiative properties of the condensed dust play a critical role on top of its thermodynamic properties. The photons radiated by the star will interact with the dust: a fraction of the light will be reflected while another fraction will be absorbed, and the last fraction is transmitted. If the fraction of absorbed light is significant, it will contribute to heating the dust to a temperature that could be higher than the temperature of the ambient gas. In turn, this higher temperature could delay dust condensation. This effect will contribute to increasing the oversaturation of this phase. As the gas and dust flow away from the star, the temperature and pressure will decrease such that at some point the predicted dust temperature shall correspond to its condensation temperature[39,40]. At this radial distance the dust can condensate.

In detail, the fraction of absorbed light depends critically on the optical parameters of the dust, and it has been shown in numerous studies that this depends on the Fe content among other parameters. When the Fe content increases, the absorption coefficient increases especially in the frequency domain where radiations are efficient at heating the material. In the case of small dust particles (µm scale), the parameter used to describe light absorption is Q_{abs} and by plotting Q_{abs}/a, where a is the diameter of the grain, as a function of photon energy, one can define a parameter p that is then used to calculate a dust temperature T_d[40]. The parameter p has been calculated for several oxides and for amorphous carbon but not for the mineral phases that are predicted to condense in high C/O environment. Based on published optical properties of FeSi,

TiC, AlN, SiC and graphite we have calculated the value of parameter p to be able to predict the corresponding dust temperature.

Ref[40] has shown that the distance of condensation of a particular mineral species can be calculated based on the value of the parameter p and the temperature at the surface of the star T^*:

$$T_d(r) = T^* \left(\frac{2r}{R^*}\right)^{-\frac{2}{4+p}} \qquad (1)$$

If the condensation temperature T_c is known independently from thermodynamic calculations, it is then possible to determine the radial distance for condensation of a particular mineral phase by setting:

$$T_d(r) = T_c(r) \qquad (2)$$

For the purpose of our calculations, we have used the *T(r)* and *P(r)* curves for a C-rich star given in ref[14] and the results of our condensation calculations are presented graphically in figure 6.

E. Calculations of parameter p for mineral phases condensed at high C/O ratio

The value of p was calculated for the following mineral phases based on published optical properties: TiC, AlN, CaS and FeSi. In the case of FeSi, the value of α_{abs} the absorption coefficient was calculated using the following equation that depends on the band gap energy[66]:

$$\alpha_{abs} = \frac{A}{\omega}\sqrt{\omega - E_g}$$

Where E_g is the band gap energy. In the case of FeSi which is a semi-conductor at low temperature but a metal at high temperature, the dependence of E_g on temperature was taken into account with the following equation[67]:

$$E_g = E_{g0} - Sh\omega.\left(coth\left(\frac{h\omega}{2kT}\right) - 1\right)$$

The value of k, the imaginary part of the refraction index, was then calculated as:

$$k(\lambda, T) = \frac{\alpha_{abs}\lambda}{4\pi}$$

Then, the value of the reflectivity given in ref[68] was used to calculate the value of the real part of the complex refraction index *(n+ik)* using the following equation:

$$R = \frac{(n-1)^2 + k^2}{(n+1)^2 + k^2}$$

Finally, the absorption parameter Q_{abs} was calculated using the following expression[69]:

$$Q_{abs} = 4\frac{2\pi a}{\lambda}\frac{6nk}{(n^2 - k^2 + 2)^2 + 4n^2k^2}$$

In the case of CaS, the experimental studies reported values of the real and imaginary dielectric function as a function of energy[70]. These parameters are directly related to the real ε_1 and imaginary ε_2 part of the complex refraction index:

$$\varepsilon_1 = n(\omega)^2 - k(\omega)^2$$
$$\varepsilon_2 = 2n(\omega)k(\omega)$$

From these equations, one can calculate:

$$k(\omega) = \sqrt{\frac{\sqrt{\varepsilon_1^2 + \varepsilon_2^2} - \varepsilon_1}{2}}$$

$$n(\omega) = \sqrt{\frac{\sqrt{\varepsilon_1^2 + \varepsilon_2^2} + \varepsilon_1}{2}}$$

The equation given above is then used to calculate Q_{abs}. In the case of TiC, the absorbance was directly determined by ab initio calculation[71]. For AlN, the value of Q_{abs} is a function of frequency that was directly calculated from the equation based on n and k, as given in ref[72].

F. Modeling the timescale of grain growth relative to the timescale of outflows

The time necessary to grow a dust grain starting from seed such as a more refractory grain highly depends on the local density of the constitutive atoms of the considered dust. If one takes the example of FeSi (Extended Data Fig. 5), then the growth rate will be limited by the rate at which individual atoms hit the grain surface. In the case of dust condensation in stellar outflow, we calculated the maximum rate of condensation by neglecting the rate of evaporation. In all cases, our calculated rates should be greater than the actual rates. As detailed in ref[34,41], the condensation rate of FeSi is limited by the rate of Si abundance since it is lower than that of Fe. One can thus write the timescale of grain growth as:

$$\frac{da}{dt} = \frac{V_0 \alpha \left(P_{Si} - P_{Si,sat}\right)}{\sqrt{2\pi m_{Si} RT}}$$

Where V_0 is the average volume occupied by a FeSi unit.

This relation can be further modified following the study of ref[41] by including the relationship between the local pressure, the density of the gas and the Si abundance:

$$P_{Si} = \frac{n_{Si}}{n_H} \frac{2n_{H_2} RT}{V} = \varepsilon_{Si} \rho RT$$

In order to calculate the growth timescale as a function of distance from the star, one can use the equation given in ref[34]:

$$\tau_{growth} = \frac{a}{\frac{da}{dt}} = \frac{a\sqrt{2\pi m_{Si} RT}}{V_0 \alpha P_{Si}} = \frac{a\sqrt{2\pi m_{Si} RT}}{V_0 \alpha \varepsilon_{Si} \rho RT} = \frac{2a}{V_0 \alpha \varepsilon_{Si} \rho(r)} \sqrt{\frac{2\pi m_{Si}}{RT}}$$

One can also calculate the timescale associated with the stellar outflow. According to ref[47] this parameter can be evaluated with the following equation:

$$\tau_{outflow} = \frac{2}{\Gamma - 1} r \frac{v}{v_{esc}^2}$$

Where Γ is defined as the ratio of radiative acceleration to gravitational attraction ref[73]:

$$\Gamma = \frac{f_K L_*}{4\pi c G M_*}$$

This parameter is increasing outwards and is above 1, ranging between 2 and 5[38] and v_{esc} is the escape velocity:

$$v_{esc} = \sqrt{\frac{2GM^*}{4R^*}}$$

The velocity of the outflow at an infinite distance can be calculated with the following equation[38]:

$$v = \sqrt{\frac{2GM^*}{r_0}(\Gamma - 1) + v_0^2}$$

Where r_0 represents the radius where the acceleration starts (the dust condensation radius). According to ref[38] the initial velocity at R^* can be approximated as the sound velocity[74] that can be defined as:

632 $$v_0 = \sqrt{\frac{C_p^{H_2} RT}{M_{H_2}\left(C_p^{H_2} - R\right)}}$$

633 The value of Cp for H_2 was taken from the NIST compilation by ref[75]:
634

635 $$C_P^{H_2} = 18.563083 + 12.257357 \times T - 2.859786 \times T^2 + 0.268238 \times T^3 + \frac{1.977990}{T^2}$$

Acknowledgements

We are particularly grateful to Frederic Fabry (PERSEE, Mines ParisTech, Nice) for his assistance in running the plasma torch. We are grateful to Susan Höfner for her insightful advice at the early stages of this project, and Marc Chaussidon for discussions. The project was financially supported by fundings from the Fédération de Recherche Wolfgang Doeblin, FR 2800, and the Université Côté d'Azur through its Academy of Complex Systems (GL). This study also received partial support from the ERC-funded project COSMOKEMS #694819.

Author information

G.L. designed the research and performed the experiments with L.F., V-J.R., C.G. and F.C. G.L, C.G, V. G. and P. V. determined the mineralogy of the condensates. M.M., B.B. and G.L. reduced the data and did the thermodynamic calculations and models. G.L. M.M. and B.B. wrote the manuscript under the supervision of E.L for AGB implications.

Data availability

All data needed to evaluate the conclusions in the paper are present in the paper and in the Supplementary Information. Additional data related to this paper may be requested from the authors.

References

1. Whittet, D.C.B. Dust in the Galactic Environment. (IOP Publishing, Bristol, UK, Third Edition, 2022).

2. Kemper, F., Vriend, W. J., & Tielens, A. G. G. M. The absence of crystalline silicates in the diffuse interstellar medium. *Astrophys. J.*, **609**, 826 (2004).

3. Höfner, S. & Olofsson, H. Mass loss of stars on the asymptotic giant branch. *Astron. Astrophys. Rev*. **26**, 1 (2018).

4. Freytag, B. & Höfner, S. Global 3D radiation-hydrodynamical models of AGB stars with dust-driven winds. *Astronomy and Astrophysics* **53**, 669 (2023).

5. Höfner, S. Starlight and Sandstorms: Mass Loss Mechanisms on the AGB In: *Why Galaxies Care about AGB Stars II: Shining Examples and Common Inhabitants*, **445**, 193 (2011).

6. Iben, I. & Renzini, A. Asymptotic giant branch evolution and beyond. *Annual Review of Astronomy and Astrophysics* **21**, 83 (1986).

7. Luo, Y. R. Comprehensive handbook of chemical bond energies. CRC Press. (2007).

8. Decin, L. et al. Water content and wind acceleration in the envelope around the oxygen-rich AGB star IK Tauri as seen by Herschel/HIFI, *Astron. Astrophys.* **521**, L4 (2010).

9. Sloan, G. C., Little-Marenin, I. R., & Price, S. D. The carbon-rich dust sequence: infrared spectral classification of carbon stars. *The Astronomical Journal* **115**, 809 (1998).

10. Speck, A.K., Corman, A.B., Wakeman,K, Wheeler, C.H., & Thompson, G. Silicon carbide absorption features: dust formation in the outflows of extreme carbon stars. *Astrophys. J.* **691** 1202 (2009).

11. Anders, E. & Zinner, E. (1993). Interstellar grains in primitive meteorites: Diamond, silicon carbide, and graphite. *Meteoritics*, 28(4), 490-514.

12. Nittler, L. R. & Ciesla, F. Astrophysics with extraterrestrial materials. *Annual Review of Astronomy and Astrophysics*, **54**, 53 (2016).

13. Gail, H. P. & Sedlmayr, E. Physics and chemistry of circumstellar dust shells. (Cambridge University Press, 2013).

14. Agúndez, M., Martínez, J. I., de Andres, P. L., Cernicharo, J., & Martín-Gago, J. A. Chemical equilibrium in AGB atmospheres: successes, failures, and prospects for small molecules, clusters, and condensates. *Astron. Astrophys.* **637**, A59 (2020).

15. Woitke, P. 2D models for dust-driven AGB star winds. *Astron. Astrophys.* **452**, 537 (2006).

16. Tielens, A. G. G. M. Dust formation in astrophysical environments: the importance of kinetics, *Front. Astron. Space Sci., Sec. Astrochemistry*, **9** (2022).

17. Ebel, D. S. Condensation of rocky material in astrophysical environments. In *Meteorites and the Early Solar System II*, 253 (2006).

18. Tsuchiyama, A., Takahashi, T., & Tachibana, S. Evaporation rates of forsterite in the system Mg_2SiO_4–H_2. *Mineralogical Journal*, **20**, 113 (1998).

19. Tachibana, S. et al. Kinetic condensation and evaporation of metallic iron and implications for metallic iron dust formation. *Astrophys. J.*, **736**, 16 (2011).

20. Matsuno, J. et al. Condensation of Glass with Multimetal Nanoparticles: Implications for the Formation Process of GEMS Grains. *Astrophys. J.*, **911**, 47 (2021).

21. Kim, T. H. et al. Condensation of cometary silicate dust using an induction thermal plasma system I. Enstatite and CI chondritic composition? *Astron. Astrophys.* **656**, A42 (2021).

22. Nuth III, J. A., Rietmeijer, F. J., & Hill, H. G. Condensation processes in astrophysical environments: The composition and structure of cometary grains. *Meteoritics & Planetary Science*, **37**, 1579 (2002).

23. Toppani, A. et al. A 'dry' condensation origin for circumstellar carbonates. *Nature*, **437**, 1121 (2005).

24. Toppani, A., Libourel, G., Robert, F., & Ghanbaja, J. Laboratory condensation of refractory dust in protosolar and circumstellar conditions. *Geochim. Cosmochim. Acta*, **70**, 5035 (2006).

25. Kimura, Y. Tanaka, K. K., Inatomi, Y., Aktas, C. & Blum, J. Nucleation experiments on a titanium-carbon system imply nonclassical formation of presolar grains, *Science Adv*. 9, eadd8295 (2023).

26. Gautier, M., Rohani, V., & Fulcheri, L. Direct decarbonization of methane by thermal plasma for the production of hydrogen and high value-added carbon black, *International Journal of Hydrogen Energy*, **42**, 28140 (2017).

27. Lodders, K. & Fegley, Jr. B. The origin of circumstellar silicon carbide grains found in meteorites, *Meteoritics*, **30**, 661 (1995).

28. Ebel, D. S. Variations on solar condensation: Sources of interstellar dust nuclei, *J. Geophys. Res.*, **105**, 10363 (2000).

29. Gobrecht, D. et al. Nucleation of Small Silicon Carbide Dust Clusters in AGB Stars, *Astrophys. J*. **840**, 117 (2017)

30. Boulangier, J., Gobrecht, D., Decin, L., de Koter, A., & Yates, J. Developing a self-consistent AGB wind model:II. Non-classical, non-equilibrium polymer nucleation in a chemical mixture, *Monthly Notices of the Royal Astronomical Society*, **489**, 4890 (2019).

31. Yoshikawa, T., Kawanishi, S., & Tanaka, T. Solution growth of silicon carbide using Fe–Si solvent. *Jpn. J. Appl. Phys.*, **49**, 051302 (2010).

32. Namur, O., Collinet, M., Charlier, B., Grove, T. L., Holtz, F., & McCammon, C. Melting processes and mantle sources of lavas on Mercury, *Earth Planet. Sci. Lett.*, **439**, 117 (2016).

33. Asplund, M., Grevesse, N., Jacques Sauval, A., & Scott, P. The chemical composition of the Sun. *Annual Review of Astronomy and Astrophysics*, **47**, 481 (2009).

34. Ferrarotti, A. S. & Gail, H.-P. Mineral formation in stellar winds III. Dust formation in S stars, *Astron. Astrophys.*, **382,** 256 (2002).

35. Karakas, A.I. & Lattanzio, J.C. The Dawes Review 2: Nucleosynthesis and Stellar Yields of Low- and Intermediate-Mass Single Stars. *Publications of the Astronomical Society of Australia* **31**, e030, 62 (2014).

36. Deutsch, A. J. The circumstellar envelope of alpha herculis. *Astrophys. J.*, **123**, 210 (1956).

37. Sedlmayr, E. & Dominik, C. Dust Driven Winds. *Space Science Reviews*, 73, 211 (1995)

38. Höfner, S. Winds of M-type AGB stars driven by micron-sized grains, *Astron. Astrophys.*, **491**, L1-L4 (2008).

39. Bladh, S. & Höfner, S. Exploring wind-driving dust species in cool luminous giants - I. Basic criteria and dynamical models of M-type AGB stars, *Astron. Astrophys.*, **546**, A76 (2012).

40. Lamers, H., & Cassinelli, J. Introduction to Stellar Winds. Cambridge: Cambridge University Press. (2012).

41. Gail, H. in *Astromineralogy*, edited by T. K. Henning, Lecture Notes in Physics (Berlin: Springer), **609**, 55 (2003).

42. Ferrarotti, A., Gail, H. -P., Degiorgi, L., Ott, H. R. FeSi as a possible new circumstellar dust component, *Astronomy and Astrophysics*, **357**, L13-L16 (2000).

43. Speck, A. K., Corman, A. B., Wakeman, K., Wheeler, C. H., & Thompson, G. Silicon carbide absorption features: dust formation in the outflows of extreme carbon stars**.** *Astrophys. J.*, **691**, 1202 (2009).

44. De Beck, E., & Olofsson, H. The surprisingly carbon-rich environment of the S-type star W Aql. *Astron. Astrophys.*, **642**, A20 (2020).

45. Volk, K., Sloan, G. C., & Kraemer, K. E. The 21 μm and 30 μm emission features in carbon-rich objects. *Astrophysics and Space Science*, **365**, 1 (2020).

46. Sloan, G. C. et al. Carbon-rich dust past the asymptotic giant branch: aliphatics, aromatics, and fullerenes in the magellanic clouds. *Astrophys. J.*, **791**, 28 (2014).

47. Marini, E., Dell'Agli, F., Groenewegen, M. A. T., García–Hernández, D. A., Mattsson, L., Kamath, D., Ventura, P., D'Antona, F. & Tailo, M. (2021). Understanding the evolution and dust formation of carbon stars in the Large Magellanic Cloud via the JWST *Astron. Astrophys.*, *647*, A69.

48. Amari, S., Zinner, E., & Gallino, R. Presolar graphite from the Murchison meteorite: An isotopic study. *Geochim. Cosmochim. Acta*, **133**, 479 (2014).

49. Wopenka, B., Yu, X. C., Zinner, E., & Amari, S. Murchison presolar carbon grains of different density fractions: A Raman spectroscopic perspective. *Geochim. Cosmochim. Acta*, **106**, 463 (2013).

50. Bernatowicz, T. J., Amari, S., Zinner, E. K., & Lewis, R. S. Interstellar grains within interstellar grains. *Astrophys. J.*, **373**, *L73* (1991).

51. Bernatowicz, T. J., Amari, S., & Lewis, R. S. Refractory carbides in interstellar graphite. In *Lunar and Planetary Science Conference*, **25**, 103 (1994).

52. Bernatowicz, T. J., Cowsik, R., Gibbons, P. R, Lodders, K., Fegley, B., Amari, S., & Lewis, R. S. (1996). Constraints on Stellar Grain Formation from Presolar Graphite in the Murchison Meteorite. *Astrophys. J.*, **472**, 760 (1996)

53. Singerling, S. A., Liu, N., Nittler, L. R., Alexander, C. O. D., & Stroud, R. M. TEM analyses of unusual presolar silicon carbide: Insights into the range of circumstellar dust condensation conditions. *Astrophys. J.*, **913**(2), 90 (2021).

54. Nittler, L. R. Presolar stardust in meteorites: recent advances and scientific frontiers. *Earth Planet. Sci. Lett.*, **209**, 259 (2003).

55. Croat, T. K., Bernatowicz, T. J., & Jadhav, M. (2014, September). Isotopic Anomalies Preserved Within Internal Grains in High-Density Presolar Graphites. In *77th Annual Meeting of the Meteoritical Society* (Vol. 77, No. 1800, p. 5354).

56. Hynes, K. M, K. Croat, T. K., Amari, S., Mertz, A. F. & Bernatowicz, T. J., Structural and isotopic microanalysis of presolar SiC from supernovae. *Meteoritics*, **45**, 596 (2010).

57. Gyngard, F., Amari, S., Zinner, E., & Marhas, K. K. (2018). Correlated silicon and titanium isotopic compositions of presolar SiC grains from the Murchison CM2 chondrite. *Geochim. Cosmochim. Acta*, **221**, 145 (2018).

58. Kodolányi, J., Vollmer, C., Hoppe, P., & Müller, M. Structural Investigation of Silicon Carbide X Grains: Constraints on Condensation in Supernova Ejecta. *Astrophys. J.*, **868(1)**, 34 (2018).

59. Decin, L., Montarges, M., Richards, A. M. S., Gottlieb, C. A., et al. (Sub-)stellar companions shape the winds of evolved stars. *Science*, **369**, 1497 (2020).

60. Bale, C.W., Belisle, E., Chartrand, P., Decterov, S.A., Eriksson, G., Gheribi, A.E., Hack, K., Jung, I.H., Kang, Y.B., Melançon, J., Pelton, A.D., Petersen, S., Robelin, C., Sangster, J., Spencer, P., Van Ende, M.A. FactSage thermochemical software and databases, 2010-2016. Calphad: *Computer Coupl. Phase Diagrams Thermochem.* **54**, 35 (2016).

61. Alexander, C. O. D. Chemical equilibrium and kinetic constraints for chondrule and CAI formation conditions. *Geochim. Cosmochim. Acta*, **68**, 3943 (2004).

62. Nagahara, H., Ozawa, K., & Tomomura, S. Kinetic condensation of silicate melt and its role in the chemical diversity of chondrules. In *Chondrites and the Protoplanetary Disk*, **341**, 456 (2005).

63. Richter, F. M., Davis, A. M., Ebel, D. S. & Hashimoto, A. Elemental and isotopic fractionation of Type B calcium-, aluminum-rich inclusions: Experiments, theoretical considerations, and constraints on their thermal evolution, *Geochim. Cosmochim. Acta*, **66**, 521 (2002).

64. Fedkin, A. V., Grossman, L., & Ghiorso, M. S. Vapor pressures and evaporation coefficients for melts of ferromagnesian chondrule-like compositions, *Geochim. Cosmochim. Acta*, **70**, 206 (2006).

65. Zeidler, S., Posch, T., Mutschke, H., Richter, H. , & Wehrhan O. Near-infrared absorption properties of oxygen-rich stardust analogues: The influence of colouring metal ions, *Astron. Astrophys.*, **526**, A68 (2011).

66. Udono, H., Kikuma, I., Okuno, T., Masumoto, Y., Tajima, H., & Komuro, S. Optical properties of h-$FeSi_2$ single crystals grown from solutions. *Thin Solid Films*, 461, 182 (2004).

67. O'Donnell, K. P. & Chen, X. Temperature dependence of semiconductor band gaps, *Appl. Phys. Lett.*, **58**, 2924 (1991).

68. Paschen, S., Felder, E., Chernikov, M. A., Degiorgi, L., Schwer, H., Ott, H. R., Young, D. P. , Sarrao, J. L. & Fisk, Z. Low-temperature transport, thermodynamic, and optical properties of FeSi, *Phys. Rev.*, **B 56**, 12916 (1997).

69. Zeidler, S., Posch, T., Mutschke, H., Richter, H., & Wehrhan, O. Near-infrared absorption properties of oxygen-rich stardust analogues: The influence of colouring metal ions, *Astron. Astrophys.*, **526**, A68 (2011).

70. Shaukat, A., Saeed, Y., Ikram, N., & Akbarzadeh H. First principles calculations of structural, electronic and optical properties of various phases of CaS. *Eur. Phys. J.*, **B 62**, 439 (2009).

71. Kim, W., Mesbah, A., Deschanels, X., Bernard, S., & Lebegue, S. First principles investigations of the optical selectivity of titanium carbide-based materials for concentrating solar power applications. *Journal of Materials Chemistry C*, **9 (24)**, 7591 (2021).

72. Jones, D. J., French, R. H., Müllejans, H., Loughin, S., Dorneich, A. D. & Carcia, P. F. Optical properties of AlN determined by vacuum ultraviolet spectroscopy and spectroscopic ellipsometry data. *J. Mater. Res.*, **14**, 4337 (1999).

73. Lamers, H., & Cassinelli, J. Introduction to Stellar Winds. Cambridge: Cambridge University Press (1999).

74. Lewis, J. S. Physics and chemistry of the Solar System, *Academic Press*, 556 pp (1995).

75. Chase, M. W. Jr., NIST-JANAF Themochemical Tables, Fourth Edition, *J. Phys. Chem. Ref. Data*, **9**, 1951 pp (1998).

76. Papoular, R. J., & Papoular, R. Some optical properties of graphite from IR to millimetric wavelengths. *Monthly Notices of the Royal Astronomical Society*, **443,** 2974-2982 (2014).

77. Pégourié, B. Optical properties of alpha silicon carbide. *Astron. Astrophys.*, **194**, *335-339*, (1988).

78. Jäger, C., Dorschner, J., Mutschke, H., Posch, T., & Henning, T. Steps toward interstellar silicate mineralogy-VII. Spectral properties and crystallization behaviour of magnesium silicates produced by the sol-gel method. *Astron. Astrophys.*, **408**, 193-204 (2003).

79. Alao, A. A., Wu, W. N., & Hsu, W. D. Sticking coefficient and Si/C ratio of silicon carbide growth species on reconstructed 4H− SiC (0001¯) surface by ab-initio calculations. *Vacuum*, **205**, 111414 (2022).

Extended data

Extended Data Table 1 Chemical Composition:

Chemical compositions in wt % of the chondrite starting material and of the bulk composition of sampled condensates shown in Extended Data Fig. 1.

		Chemistry	**Si**	**Al**	**Fe**	**Mn**	**Mg**	**Ca**	**Na**	**K**	**Ti**	**P**	**O**	C	S
		NWA 869 chondrite bulk composition	**19.28**	**1.20**	**19.01**	**0.28**	**15.24**	**1.54**	**0.69**	**0.10**	**0.07**	**0.11**	**43.28**	**0.12**	**2.38**
		Det. Limit	*0.02*	*0.02*	*0.01*	*0.01*	*0.02*	*0.02*	*0.01*	*0.02*	*0.01*	*0.04*			
Calculated average temperature* in K	# sample from top of T-rod	Depth of sampling in mm													
2308	#14	0-50	24.95	0.16	42.81	0.02	0.03	0.09	< d.l.	< d.l.	0.14	< d.l.		26.28 ^	0.04
2142	#13	50-100	26.59	0.24	44.40	0.02	< d.l.	0.07	< d.l.	< d.l.	0.14	< d.l.		23.55 ^	0.04
2042	#12	100-150	31.61	0.79	57.07	0.12	< d.l.	0.06	< d.l.	< d.l.	0.25	< d.l.		2.59 ^	0.02
1949	#11	150-200	14.43	1.99	30.40	0.11	0.33	1.44	< d.l.	< d.l.	0.07	0.11		43.59 ^	0.43
1833	#10	200-250	13.70	1.24	18.18	0.13	8.46	1.68	< d.l.	< d.l.	0.04	0.13		38.37 ^	0.04
1741	#9	250-300	23.37	1.42	20.31	0.30	18.92	1.86	< d.l.	< d.l.	0.04	0.21		0.40	0.33
1685	#8	300-350	22.67	1.10	14.62	0.36	22.27	1.49	< d.l.	< d.l.	0.03	0.21		1.34	3.42
1615	#7	350-400	18.74	0.84	11.01	0.34	22.76	1.16	< d.l.	< d.l.	0.02	0.18		6.59	3.50
1556	#6	400-450	15.97	0.72	8.82	0.35	22.12	1.00	< d.l.	< d.l.	0.02	0.16		8.78	3.06
1502	#5	450-500	15.38	0.70	8.09	0.39	22.05	0.98	< d.l.	< d.l.	0.02	0.15		10.06	3.08
1453	#4	500-550	15.64	0.70	7.76	0.45	22.57	0.99	< d.l.	< d.l.	0.02	0.15		10.74	3.11
1395	#3	550-600	15.88	0.71	7.74	0.51	24.32	1.01	0.02	< d.l.	0.02	0.14		10.24	3.08
1389	#2	600-650	16.36	0.73	7.87	0.52	24.81	1.05	0.03	< d.l.	0.02	0.15		9.08	3.35
1365	#1	650-700	-	-	-	-	-	-	-	-	-	-		8.23	3.08

* Temperature calculated using the ANSYS Fluent computational fluid dynamics software (see methods).

^ Carbon contamination of samples stuck to the carbon T-rod during sampling

Extended Data Table 2 Mineralogy:
Mineralogy of the condensates sampled on the T-shape graphite rod holder as determined by Scanning Electron Microscopy and X-Ray diffraction.

		Mineralogy	C	FeSi	SiC	TiC	Al_4SiC_4	CaS	MgS	AlN	TiN	Si-glass	$MgAl_2O_4$	Mg_2SiO_4	MgO	$MgSiO_3$	Notes
Calculated average temperature* in K	# sample from top of T-rod	Depth of sampling in mm															
2308	#14	0-50	-	✓	✓-6H	✓	✓										
2142	#13	50-100	-	✓	✓-6H												
2042	#12	100-150	-	✓	✓-6H			✓		✓		✓ (Al-rich)					
1949	#11	150-200	-	✓	✓-6H			✓		✓	✓	✓		✓			
1833	#10	200-250	-	✓	✓-6H							✓	✓	✓			
1741	#9	250-300	✓	✓								✓		✓			
1685	#8	300-350	✓	✓				✓	✓			✓		✓	✓	(✓)	
1615	#7	350-400	✓	✓								✓		✓	✓		
1556	#6	400-450	✓	✓								✓		✓	✓		
1502	#5	450-500	✓	✓								✓		✓	✓	✓	
1453	#4	500-550	✓	✓								✓		✓	✓	✓	
1395	#3	550-600	✓	✓								✓		✓	✓	✓	
1389	#2	600-650	✓	✓								✓		✓	✓	✓	
1365	#1	650-700	✓	✓								✓		✓	✓	✓	

Extended Data Table 3 Bulk Chemistry: Bulk composition of the starting material and values of condensation factors used in the modeling. The composition of the experiment corresponds to a C/O of 0.93 and calculated considering that 600 g of NWA869 ordinary chondrite were introduced with 4 Nm^3 of Ar and 2Nm^3 of H_2.

Element	**mass (g)**	**Phase**	***f* %**
Fe	111.5	FeSi	*8*
Mn	1.617	SiC	*3*
Ti	0.390	AlN	*5*
Ca	9.045	CaS	*2*
K	0.575	Silicate melt	*4*
Ar	7132	Aluminates	*2*
S	13.96	Olivine	*8*
P	0.648	MgO	*5*
Si	113.1	TiC	*5*
Al	7.061	Graphite	*8*
Mg	89.41		
Na	4.061		
O	248.63		
N	150		
C	173.58		
H	179.94		

Extended Data Table 4 Optical Parameter: Optical parameter p of various mineral phases.

Phase	p	Reference
Graphite	2.0	76
SiC	0.3	77
TiC	0.8	71
FeSi	2.2	68
AlN	-0.35	72
CaS	0.82	70
Mg_2SiO_4	-0.9	78
$MgSiO_3$	-0.5	39

Extended Data Fig. 1 2D Thermal Regime.
The 2D thermal regime (a) inside the chamber as well as the trajectory (b) and velocity of fictive particles (c) have been obtained using the ANSYS Fluent computational fluid dynamics software (see Methods).

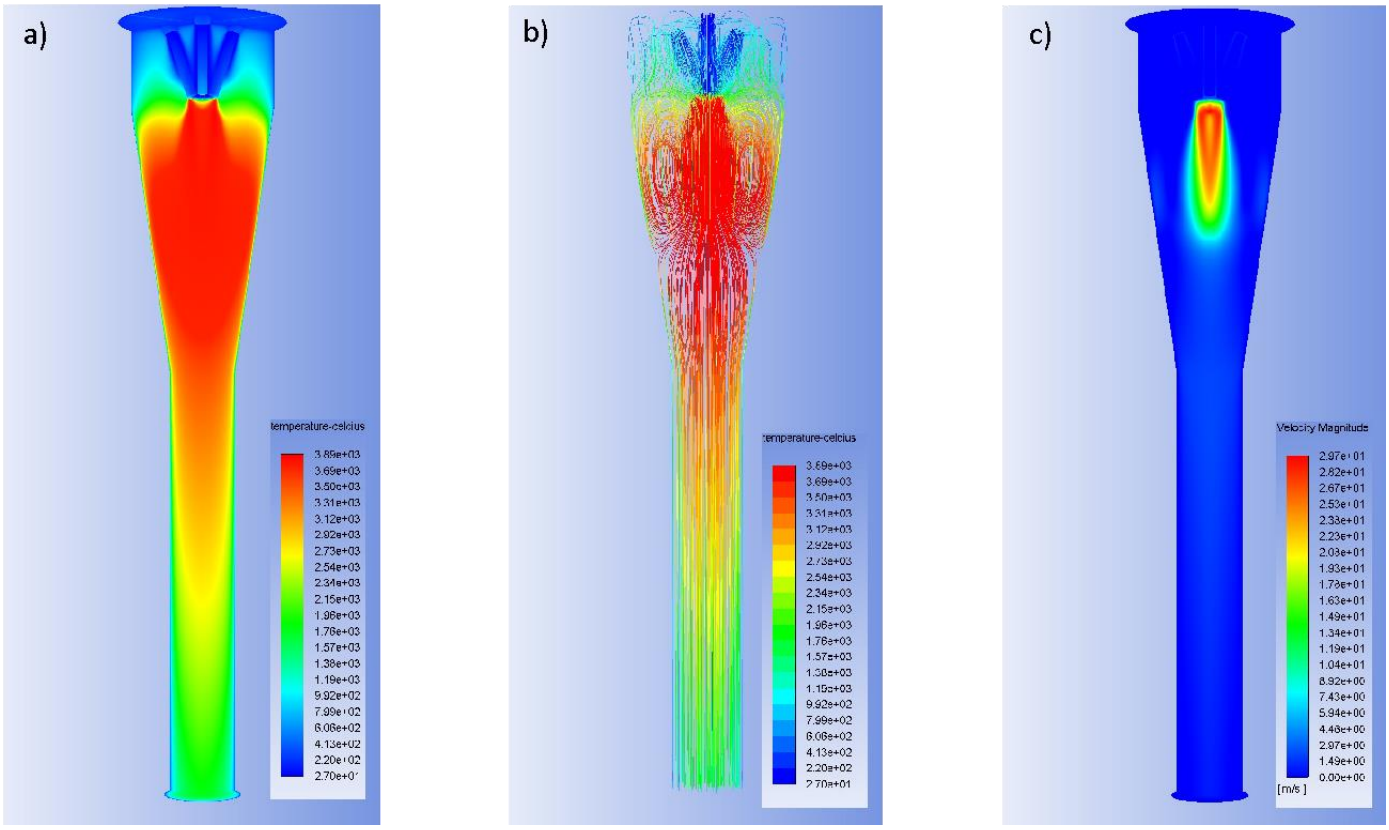

Extended Data Fig. 2 Samples.
Photograph of the graphite rod sample holder after the experiment that collected the condensates. As shown, 14 segments of 5 cm each have been sampled for bulk chemical analysis. CS1-CS6 correspond to sampling for detailed mineralogy depicted in Extended Data Fig. 3. See the chemistry and mineralogy of the condensates in Extended Data Table 1 and Table 2, respectively.

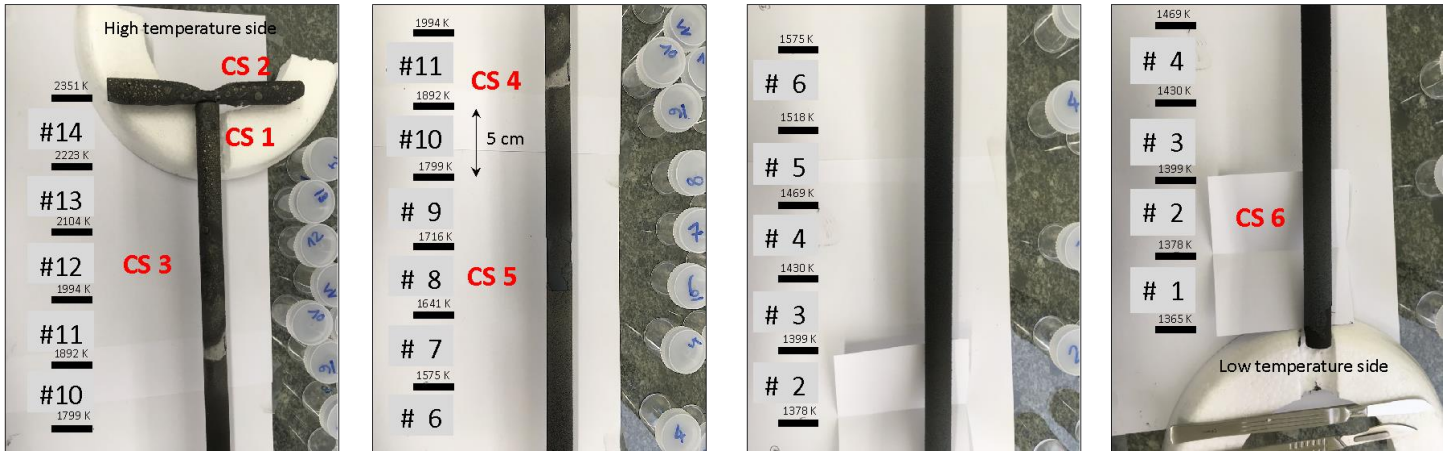

Extended Data Fig. 3 Further Mineralogy.
Further mineralogical and chemical characterization of condensed phases sampled on the graphite T-rod sample holder with location indicated on Extended Data Fig. 3. All images and analyses by scanning electron microscopy (SEM) and energy dispersive X-ray (EDX) analysis, unless specified.

CS1 and CS2 (#14)

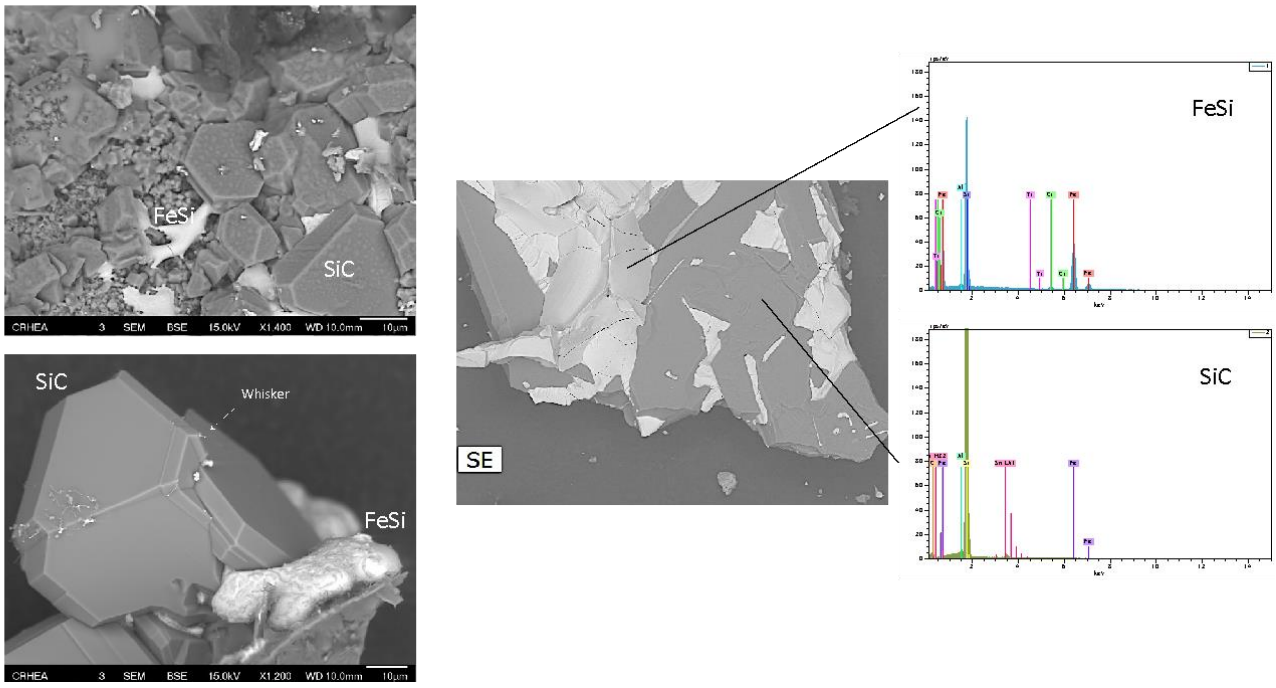

Notice in the highest temperature condensates the abundance of crystallized hexagonal SiC bathed in an iron silicide liquid, now crystallized in a mixture of naquite (FeSi), hapkeite (Fe_2Si) and possibly xifengite (Fe_5Si_3).

CS1 and CS2 (#14)

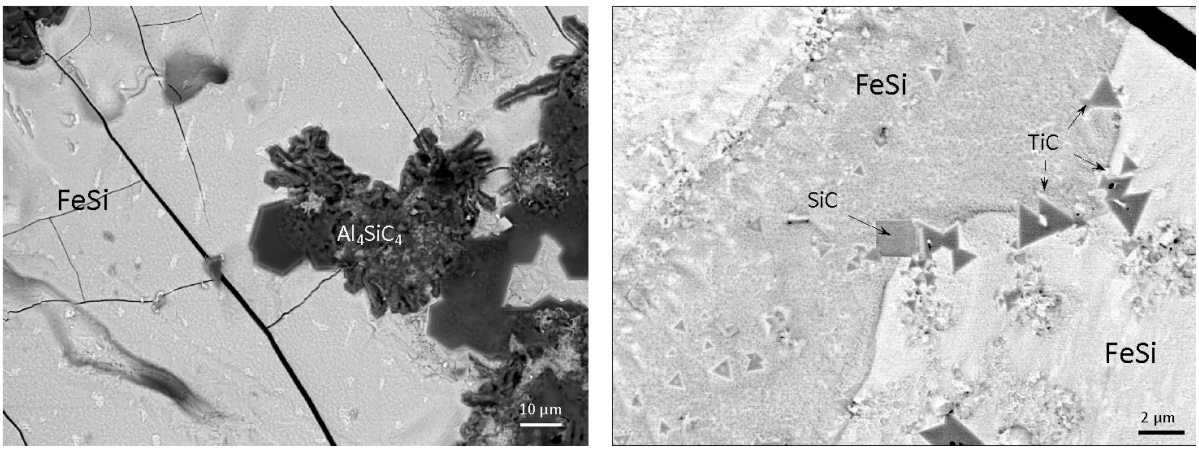

Titatium (TiC) and aluminum (Al_4SiC_4) carbides are also present in close association with the iron silicides.

CS4 (#11)

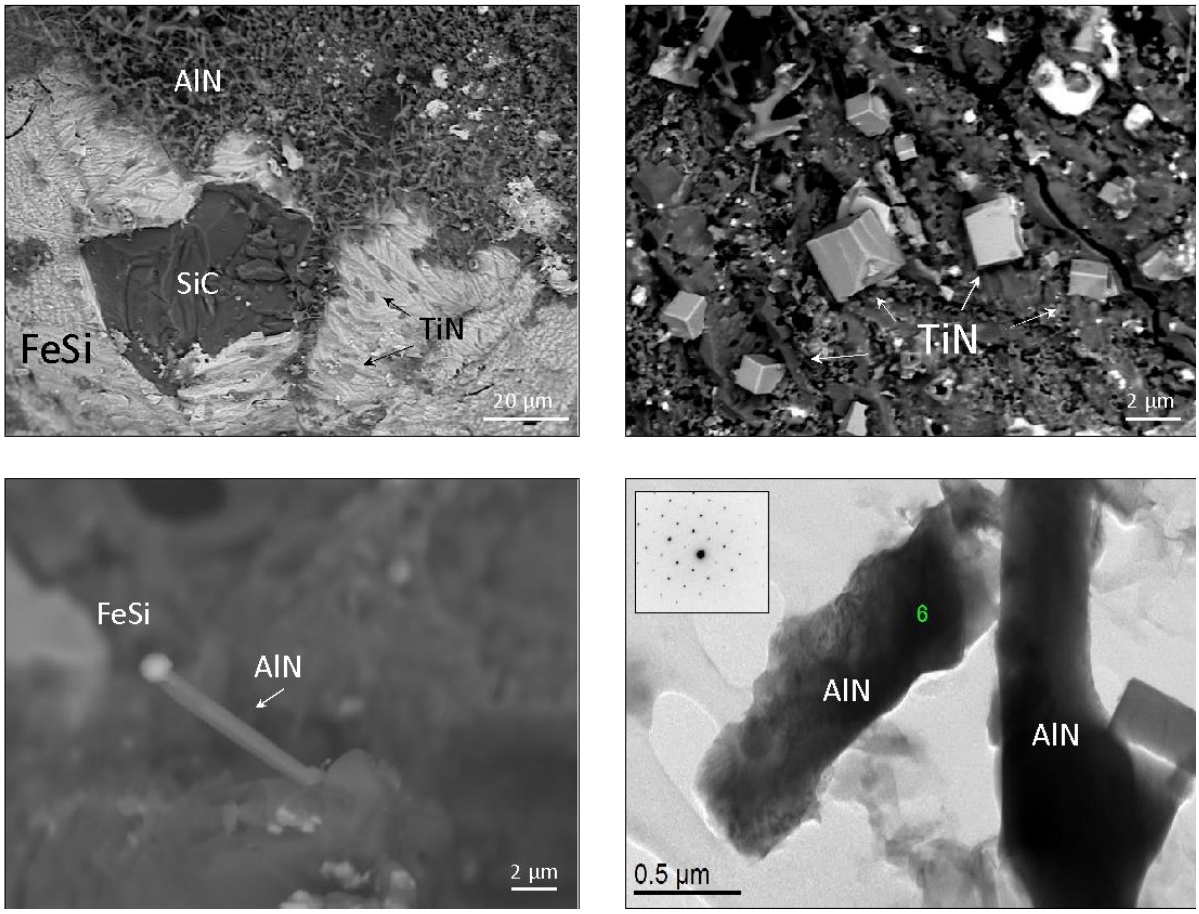

Intermediate condensates contain aluminum (AlN) and titanium (TiN) nitrides. Notice the remarkable 1-D whisker of AlN formed by a FeSi catalyst-assisted VLS (vapor-liquid-solid) growth process. All 3 first images by SEM, excepted the bottom one right which corresponds to transmission electron microscopy (*TEM*) analysis and the obtained diffraction pattern of AlN.

CS4 (#11)

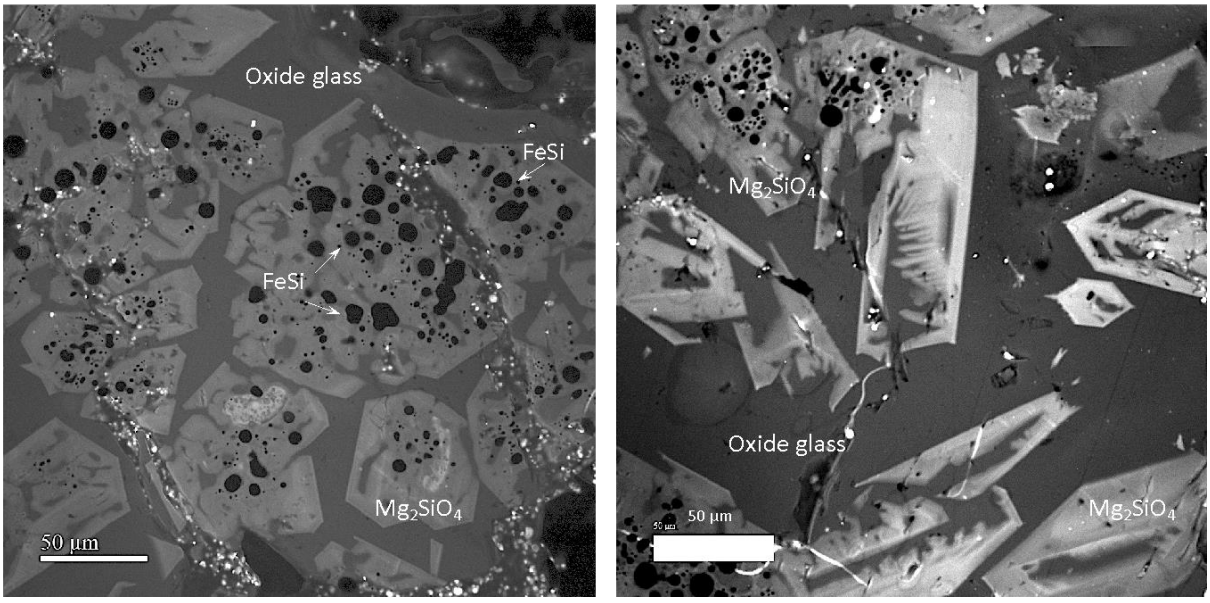

Between 2000-1900 K Mg_2SiO_4 starts to crystallize from the melt (now glassy and enriched in MgO and SiO_2) in close association with FeSi (black beads). Panchromatic images obtained by high resolution cathodoluminescence.

CS5 (#8)

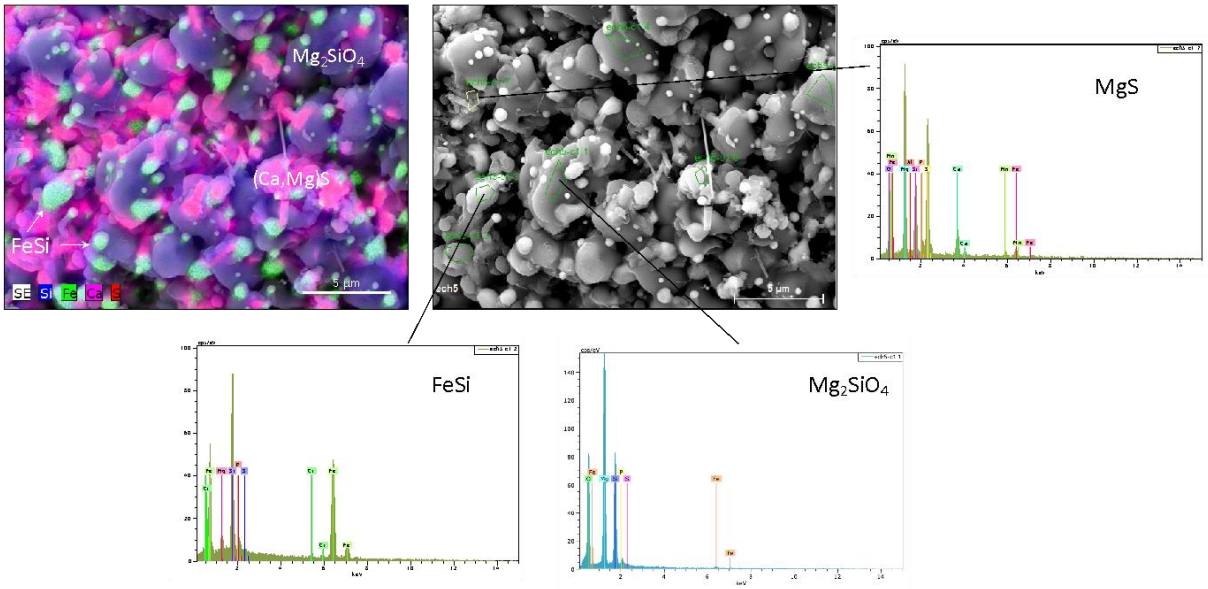

Below a temperature range of 1850-1800 K, carbides are no longer detectable, and olivine, FeSi and sulfides (Ca,Mg)S and graphite are frequently observed..

CS5 (#8)

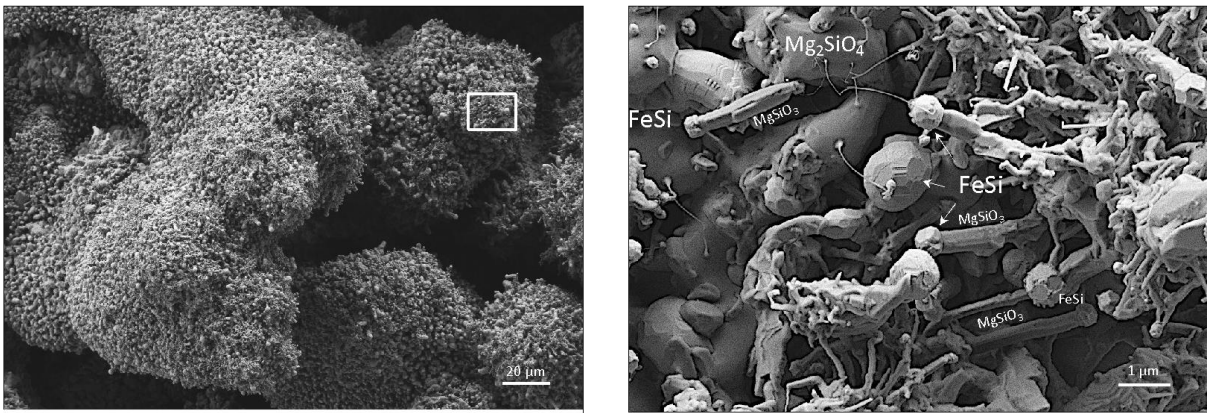

Below 1800K, the average size of condensed phases becomes micron-sized. Remarkable wiskers of enstatite are present.

CS6 (#2)

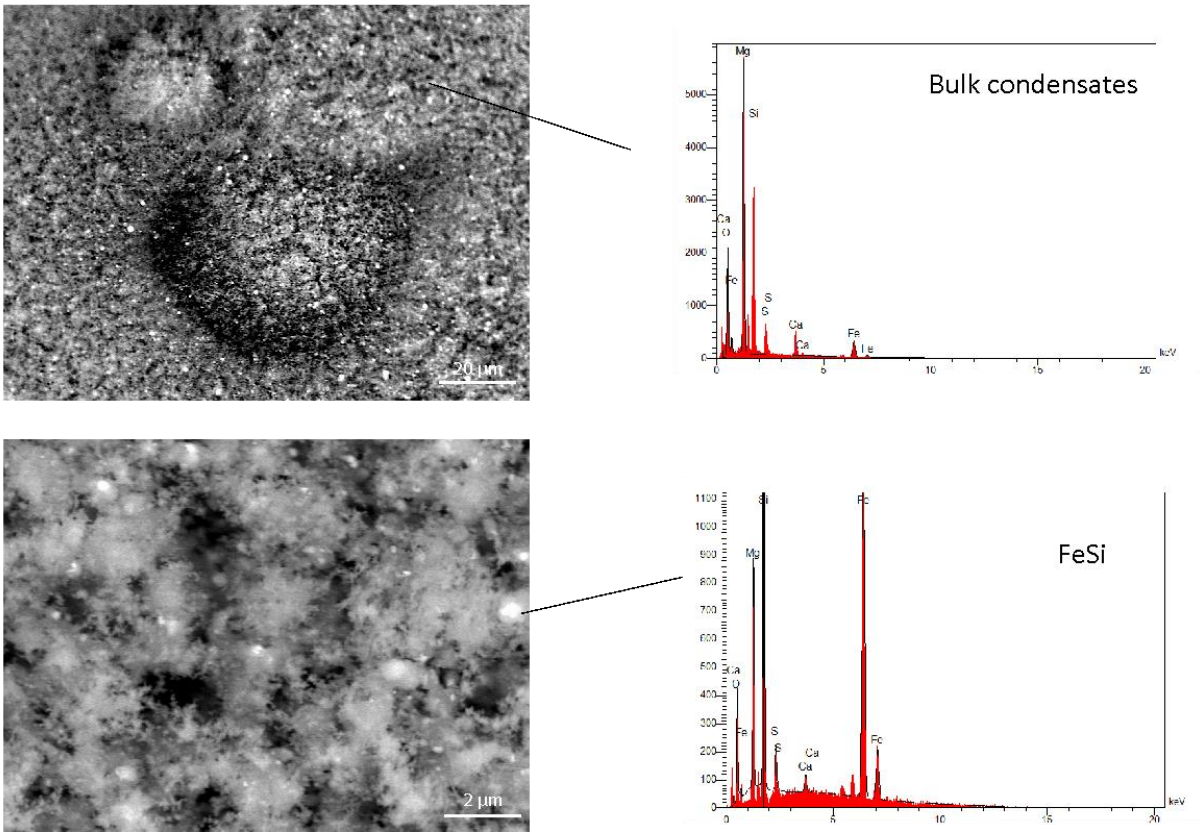

The lowest condensates on the T-shape graphite holder becomes very fine grains more difficult to identify by SEM. A bulk analysis by EDX of a few µm² of condensates reveals a composition similar to that obtained by ICP-MS on a larger sample (Fig.4).

CS6 (#2)

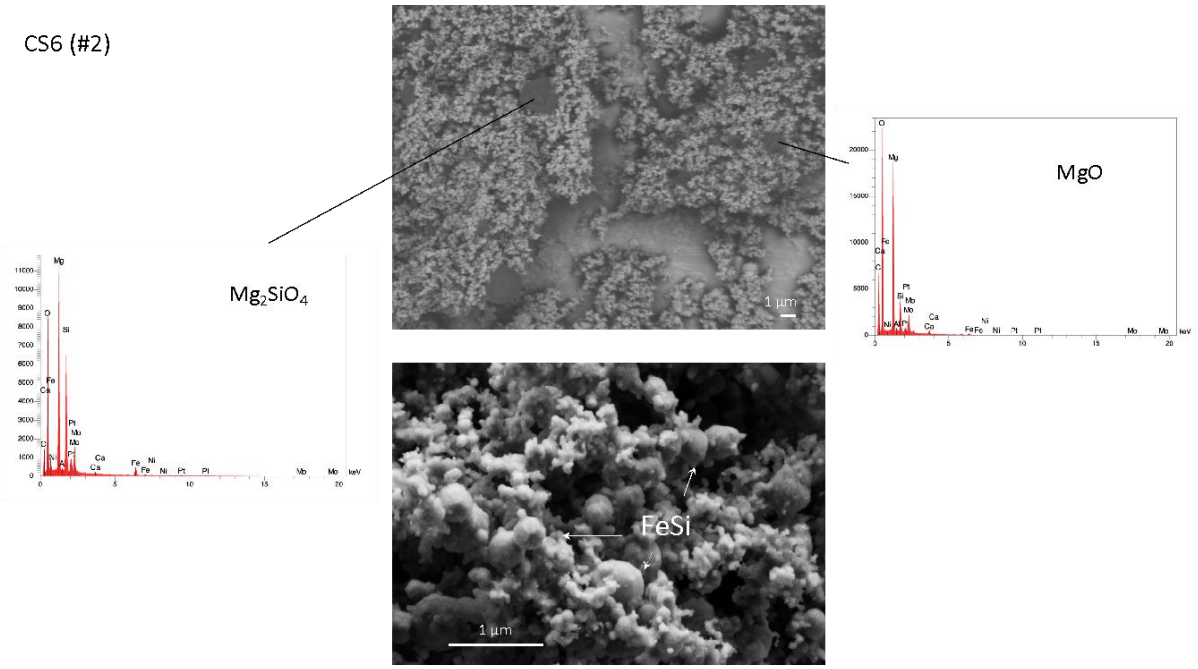

In these range of temperature circa 1400 K, the mineralogy is dominated by magnesian silicates (olivine and pyroxene), sulfides, oxides (MgO), with graphite and silicides (Fe/Si≈ 2).

Extended Data Fig. 4 Kinetic Model.
Schematic view of the kinetic model. a) The internal cylinder is the graphite rod. The total surface of evaporation corresponds to the graphite rod and the chamber's sides. b) Condensation factor of Ca (red) and Fe (blue). For temperatures higher than 1750 K, Ca partitions only in the oxide melt, then in oxide melt and CaS

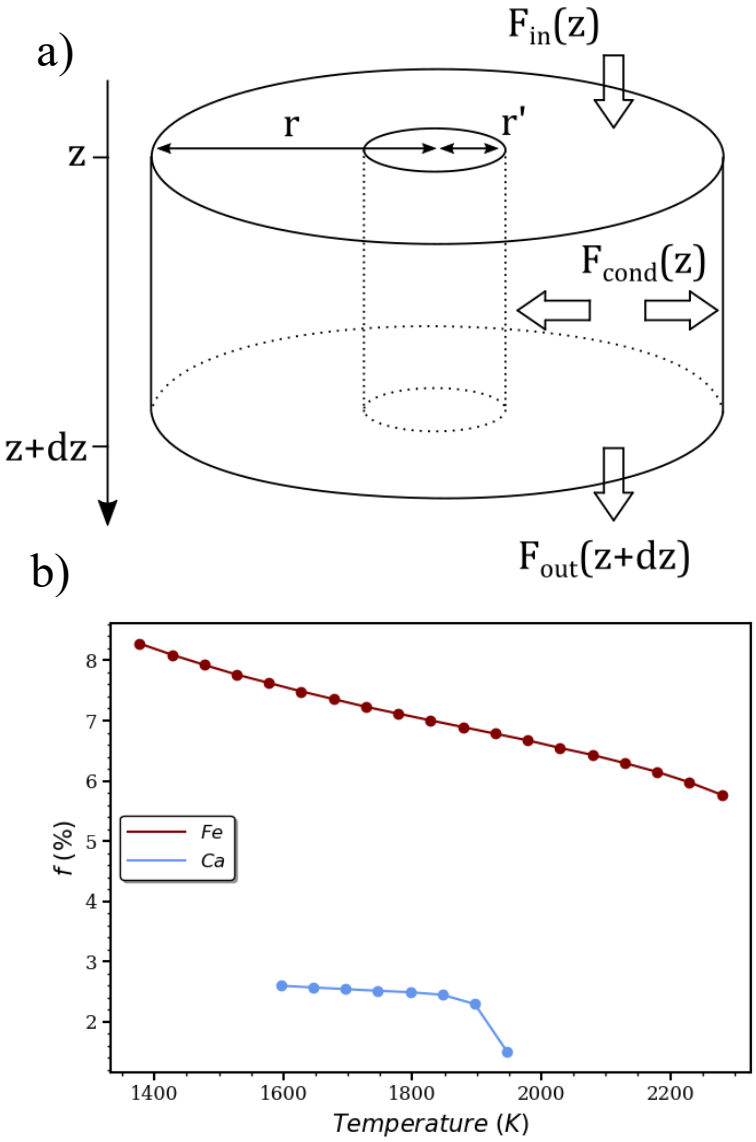

Extended Data Fig. 5 FeSi Growth Timescale.
Calculated timescales of FeSi growth (red) and stellar outflow (blue) as a function of the distance of the star (normalized to star radius R*). Red curves are for Si growth for grains with a size labeled on the curve. Assuming a larger grain diameter would lead to longer timescales. Sticking coefficient of $Si_{(g)}$ is taken from ref.[79].